Shallow Water simulations of Saturn's Giant Storms at different latitudes

E. García-Melendo[1,2], and A. Sánchez-Lavega[1]

[1] Departamento de Física Aplicada I, Escuela Técnica Superior de Ingeniería, Universidad del País Vasco UPV-EHU, Alameda Urquijo s/n, 48013 Bilbao, Spain.

[2] Fundació Observatori Esteve Duran, Montseny 46, 08553 Seva, Spain

ABSTRACT

Shallow water simulations are used to present a unified study of three major storms in Saturn (nicknamed as Great White Spots, GWS) at different latitudes, polar (1960), equatorial (1990), and mid-latitude (2010) (Sanchez-Lavega, 2004; Sanchez-Lavega et al., 2011). In our model, the three GWS are initiated by introducing a Gaussian function pulse at the latitude of the observed phenomena with controlled horizontal size and amplitude. This function represents the convective source that has been observed to trigger the storm. A growing disturbance forms when the pulse interacts with ambient winds, expanding zonally along the latitude band of the considered domain. We then compare the modeled potential vorticity with the cloud field, adjusting the model parameters to visually get the closest aspect between simulations and observations. Simulations of the 2010 GWS (planetographic latitude +40º, zonal velocity of the source -30 m s^{-1}) indicate that the Coriolis forces and the wind profile structure shape the disturbance generating, as observed, an open anticyclone with a high speed peripheral circulation and a long-lived anticyclone accompanied by strong zonal advection on the southern part of the storm forming a turbulent region. Simulations of

the equatorial 1990 GWS (planetographic latitude +12º to +5º, zonal velocity of the source 365 m s^{-1} to 400 m s^{-1}) show a different behavior because of the intense eastward jet, meridional shear at equator, and low latitude dynamics. A round shaped source forms as observed, with the rapid growth of a Kelvin-Helmholtz instability on the north side of the source due to advection and to the strong meridional wind shear, whereas at the storm latitude the disturbance grows and propagates eastward. The storm nucleus is the manifestation of a Rossby wave, while the eastward propagating planetary-scale disturbance is a gravity-Rossby wave trapped around the equator. The 1960 GWS disturbance (planetographic latitude +56º, zonal velocity 4 m s^{-1}) formed a chain of periodic oval spots that mimic the few available observations of the phenomenon. For the mid and high latitude storms, simulations predict a strong injection of negative relative vorticity due to divergence of the storm upwelling material, which may produce large anticyclones on the anticyclonic side of the zonal profile, and a quick turbulent expansion on the background cyclonic regions. In general, simulations indicate that negative relative vorticity injected by storms define the natural interaction with the zonal winds at latitudes where Coriolis forces are dominant.

1. Introduction

Saturn's planetary encircling storms, popularly known as Great White Spots (GWS) are rare events, appearing in approximate intervals of 30 years, with 6 cases reported in the last 140 years (Sanchez-Lavega, 1982, 1994; Sanchez-Lavega et al., 2011). The recorded giant storms developed at different latitudes and always in the northern hemisphere: at the equatorial region (years 1876, 1933 and 1990), mid-latitudes (1903, 2010) and at subpolar latitudes (1960) (Figure 1). Globally, the phenomenon includes in essence three phases: (1) The outbreak of a very bright "spot" that represents the onset stage; (2) The rapid growth and horizontal expansion of this "spot" reaching ~ 10,000 km in about ten days, the nicknamed GWS feature (Sánchez-Lavega, 1994); (3) The planetary-scale development of the mature disturbance (Sánchez-Lavega, 1994). The GWS's high

brightness at optical wavelengths relative to neighbouring clouds and its spectral behaviour (Sánchez-Lavega et al., 1991; Westphal et al., 1992; Acarreta and Sánchez-Lavega, 1999; Sánchez-Lavega et al., 2011; Sanz-Requena et al., 2012), together with the rapid area growing rates (expansion velocities ~ 30 m s^{-1}), are consistent with an onset driven by vigorous moist convection starting at the deep water clouds at level ~ 10 bars or ~ 250 km below visible cloud tops (Sanchez-Lavega and Battaner, 1987; Hueso and Sanchez-Lavega, 2004). This hypothesis has been recently supported by the observation of lightning events (Fisher et al., 2011) and detection of water-ice at the clouds tops of the last 2010 event (Sromovsky et al., 2013).

[Figure 1]

The evolution from a local eruption to a mature GWS planetary-scale disturbance is dictated by the ambient dynamics and zonal winds, and therefore by the outbreak latitude. Details of this stage have been studied with ground-based telescopes and with the Hubble Space Telescope in 1990 (Sanchez-Lavega et al., 1991; Beebe et al., 1992; Barnet et al., 1992) and Cassini spacecraft instruments in 2010 (Fletcher et al., 2011; Fisher et al., 2011; Sanchez-Lavega et al., 2011, 2012; Sayanagi et al., 2013). The complex cloud morphology, spanning the whole latitude of the outbreak in a few months, and the related wind field, are the main tracers of the subjacent dynamics. In addition, temperature and composition variations have been recorded for the 2010 case above cloud tops (Fletcher et al., 2011; Laraia et al., 2013).

Simulations of the dynamics at this stage have been performed using the nonlinear EPIC code (Dowling et al., 1998) modified for the case of the Equatorial 1990 GWS to incorporate mass injection (Sayanagi and Showman, 2007), and for the 2010 mid-latitude event (Sanchez-Lavega et al., 2011; García-Melendo et al., 2013). The GWS1990 simulations by Sayanagi and Showman (2007) focused on the effects of the storm on the equatorial jet, whereas those for the GWS 2010 were used to reproduce cloud

77 morphology in order to constrain the wind and temperature structure beneath the upper levels accessible
78 to remote sensing. This paper is devoted to the study and identification of the dominant rotational and
79 advective dynamical phenomena that participate in the planetary-scale disturbances that follows the
80 GWS convective outbreak by reproducing the observed cloud morphology. In particular, we analyze the
81 nature of eddies and waves that form in the disturbance and how they depend on the zonal wind field,
82 latitude and outbreak intensity. We do so with unified, more simple, one and two-layer shallow water
83 (SW) models for the three latitudes where the GWS have been observed (equator, mid- and sub-polar
84 latitudes) using as a guide the three most recently observed events (1990, 2010 and 1960, respectively).
85 The models are computationally much faster, allowing higher spatial resolution than in previous works,
86 and yet keep part of the essential dynamics of Saturn's atmosphere.
87
88 **2. A comparative view of the GWS disturbances**
89
90 The three GWS cases we study appeared at different latitudes of Saturn where planetary dynamical
91 conditions were different (zonal jets and Coriolis force, among others); therefore, their evolution was
92 different (Table 1, Figures 1 and 2). To fix conditions, we use in this paper System III reference
93 frame for wind speeds (positive eastward, Archinal et al., 2009) and planetographic latitudes (see
94 definitions in Sanchez-Lavega, 2011). We do not know what exact latitude the 1960 GWS emerged
95 at and when, but when the perturbation was discovered it had already encircled the planet and there
96 was a bright spot close to the sub-polar latitude of +58º where it drifted at +4 ms^{-1} (Dollfus, 1963;
97 Sanchez-Lavega, 1982). The 1990 storm appeared at +12º and initially the "head" (leading bright
98 spot) moved with a velocity close to the background flow of the large equatorial jet at 365 m s^{-1} (see
99 details in Sánchez-Lavega et al., 1991; Beebe et al., 1992; Barnet et al., 1992; Westphall et al., 1992;
100 Sánchez-Lavega, 1994). In two weeks the core of the storm shifted equatorward to +4º where it
101 moved at +402 ms^{-1}. The 1990 GWS was a major event that fully disturbed the equatorial region for
102 years with a resurgence of activity in 1994 (Sanchez-Lavega et al., 1996). Finally, the 2010 GWS

appeared at +41.0º, close to the peak of a westeward jet, moving at a speed of -28 m s^{-1} (Fisher et al., 2011; Sánchez-Lavega et al., 2011, 2012; Sayanagi et al., 2013; García-Melendo et al. 2013).

[Table 1]

[Figure2]

The mature phase of these storms is reached when, following their zonal expansion, they fully encircle the latitude band at both sides of the outbreak point (Figure 1). We summarize the most distinctive aspects of the three disturbances studied in this paper at the cloud tops (upper troposphere), as sensed at visible wavelengths (out of the 890 nm methane absorption band) that corresponds approximately to the altitude range between levels ~ 0.1 bar (tropopause) and ~ 1 bar (ammonia cloud deck):

(1) GWS 1960 (sub-polar). There are limited observations of this event but the most distinctive aspects were the following (Fig. 1A): (a) A main large bright spot (~ 20,000 km in zonal size) and a secondary bright spot were reported. We are not sure about the identity of the large main spot, perhaps it is associated to the convective source or to a large vortex or wave; (b) Eastward expansion of the disturbance at a speed of 60 to 75 m s^{-1} (corresponding to latitude +63º) and formation of series of spots along the band; (c) Northward expansion up to latitude +78º with a mean meridional velocity $\upsilon \sim 4$ m s^{-1}.

(2) GWS 1990 (Equatorial). During the storm onset at latitude ~ +12º, the cloud expanded quickly as an elliptical high albedo spot tilted ~ 45º with respect to the planet's equator adopting an integral-like shape (Sanchez-Lavega et al., 1991; Sánchez-Lavega, 1994; Beebe et al., 1992). This spot is identified as the storm nucleus or head due to the convective source and related cloud field. During this period the structure of the nucleus became more complex and expanded zonally dividing into

distinct spots. The overall cloud expansion of the storm was very quick reaching horizontal dimensions of ~30,000 km about one week later, and 95,000 km two weeks later after the onset. At the same time, two branches emerging from the north at ~ +16º and south at ~ +7º extremes of the ellipse-like cloud expanded zonally towards the west and east respectively. The expansion towards the west developed an irregular undulating structure. The southern branch expanded towards the east generating, according to some authors, a planetary wave near the equator (Beebe et al., 1992; Barnet et al., 1992). Both branches encircled the planet in ~20 days forming the planetary-scale disturbance (Sánchez-Lavega, 1994). The scarce HST available observations are fundamental to understand the development of the GWS into the mature state two months after the onset (Fig. 1C and 1D). In this stage, the active convective source formed an arrow-point shaped feature with an Eastward large bright spot; a secondary large spot appeared at a distance of 180º in longitude from the convective source; a turbulent wavy zonal pattern formed northwards of the head, in the latitude band from +15º to +25º. The whole disturbance spanned the ample Equatorial latitude range from -15º to +25º.

(3) GWS 2010 (mid-latitude): This is the best studied case thanks to Cassini observations (Fig. 1E-1F). The main features described bellow took place as soon as the storm outbroke and lasted until the storm's demise (for more details on the evolution of all these features see Sánchez-Lavega et al., 2012; and Sayanagi et al., 2013): (a) Since the initial outbreak of the storm, and as a result of the interaction between the convective cloud and the background zonal winds, a cloud-front formed at the edge of the spot enveloping the so-called "head". This bow-like structure enclosed an intense open anticyclone with speeds of ~ 160 ms^{-1} at periphery (García-Melendo et al., 2013); (b) Clouds injected by the storm were advected by the dominant zonal winds forming the "tail", a planetary-scale disturbance that encircled the whole planet; (c) The convective source (the storm head) persisted for 7 months being extinguished following its encounter with the planetary encircling features; (d) The Eastward expansion of the disturbance generated periodic structures with different vorticities at two main latitude circles (northern +44° and southern +32° branches of the storm); (e) A

155 long lived single anticyclone oval was generated at +41.5°; (f) During the first months of storm
156 activity, a series of small anticyclones formed in the southern branch at latitude +32°N.
157
158 In addition, the 2010 GWS disturbance modified the zonal winds around the westward jet at +40º
159 (Sayanagi et al., 2013). Such zonal wind change persisted for at least a few months after the storm's
160 demise on Cassini zonal winds measurements. In the case of the 1990 GWS, the situation is more
161 complex. The only precise measurements of Saturn's zonal winds after and before the 1990 storm at
162 the cloud top level were those performed during the Voyager era in 1981 (Ingersoll et al., 1984;
163 Sánchez-Lavega et al., 2000), and after Cassini's orbital insertion in 2004 (García-Melendo et al.,
164 2011). While the strong equatorial jet reached an intensity of ~ 450 m s^{-1} during the Voyager era,
165 Cassini observations showed that the equatorial jet had slowed down by ~100 m s^{-1} accompanied by
166 a change in the jet peak profile. Wind measurements using HST images between 1996 and 2002
167 showed a large drop in the peak velocity by ~150 m s^{-1} and a change in its shape (Sanchez-Lavega et
168 al., 2003). However, it is still not clear if these intensity changes are fully real or they are combined
169 with differences in altitude of the tracers and vertical wind shears (Porco et al, 2005; Pérez-Hoyos
170 and Sánchez-lavega, 2006). Sayanagi and Showman (2007) using the EPIC model searched for the
171 equatorial jet weakening but they did not get a significant slow down at the cloud top level, only at
172 the stratospheric 10 mbar level.
173
174 **3. The Shallow Water model**
175
176 SW models are useful tools to account for the effects of rotation and zonal jet interaction in a planet
177 atmosphere without including stratification, or a crude representation of it if more than 1 layer builds
178 up the model. On the other hand, we will have to keep in mind SW model limitations when
179 interpreting simulation results. In the context of the giant Solar System and extrasolar planets, SW
180 models have been used to study the generation and stability of zonal wind patterns including a 1½

reduced gravity and 2-layer models (see Vasavada and Showman, 2005, for a review and references therein). In these models the upper low density layer represented the "weather layer", where dynamical activity is to be studied, and a bottom denser layer mimicked the deep abyssal atmosphere of these planets (Hubbard et al, 2009). In our study we adopted 1-layer flat-bottomed and 2-layer SW models in spherical coordinates on an oblate spheroid. The 1-layer flat-bottomed model is used to strictly study rotational effects and the interaction of zonal jets with mass and energy injected by the storm. In this case zonal winds are not allowed to evolve; this is a good situation to study how advection, planetary waves, and instabilities shape storm dynamics, when zonal winds are massive and persistent. The purpose of the 2-layer model is to have a simple representation of the weather layer and the deep abyssal atmosphere and check the results against the one-layer case. In the 2-layer model, we add a height field to obtain a free surface which is in geostrophic balance with zonal winds. The bottom layer is not quiescent, and follows the height field to ensure a layer of uniform depth and therefore a Rossby radius of deformation which only depends on beta. In this second configuration we let zonal winds to interact with the storm in the simplest approach to a stratified atmosphere. In this last configuration, if zonal winds are stable, results should be similar to the 1-layer case.

The 1-layer model consisted on a flat bottomed channel with a constant-density inviscid fluid whose dynamics is described by the following equations (see e.g. Vallis, 2007):

$$\begin{cases} \dfrac{Du}{Dt} - \left(f + \dfrac{u}{r} tg\left(\varphi\right) \right) \upsilon = -\dfrac{g}{r\cos\varphi} \dfrac{\partial \eta}{\partial \lambda} \\ \dfrac{D\upsilon}{Dt} + \left(f + \dfrac{u}{r} tg\left(\varphi\right) \right) u = -\dfrac{g}{R} \dfrac{\partial \eta}{\partial \varphi} \\ \dfrac{\partial h}{\partial t} = -\nabla \bullet \left(h\mathbf{u} \right) - \dfrac{h - h_0}{\tau_R} + S\left(\lambda, \varphi, t\right) \end{cases} . \qquad (1)$$

where $\mathbf{u}=(u,\upsilon)$ is the velocity field, with u and υ the respective zonal and meridional velocities, D/Dt is the material derivative, $f=2\Omega\sin\varphi$ is the Coriolis parameter, η is surface elevation with respect to the fluid's rest level, h is the model's total layer thickness, $h-h_0/\tau_R$ is a Rayleigh dissipation term which relaxes the model to the undisturbed initial layer depth h_0 at the time rate τ_R, r is the local radius, and R is the meridional radius of curvature. On an oblate spheroid both radii are expressed, in terms of the planetographic latitude φ, as

$$\begin{cases} r(\varphi)\cos\varphi = \dfrac{R_e}{\left(1+\left(R_p/R_e\right)^2\tan^2\varphi\right)^{1/2}} \\ R(\varphi) = \dfrac{r(\varphi)}{\sin^2\varphi+\left(R_e/R_p\right)^2\cos^2\varphi} \end{cases} . \qquad (2)$$

g is the local acceleration of gravity, which in an oblate planet in rapid rotation as Saturn can be expressed as a function of planetocentric latitude φ_c as:

$$g(\varphi_c) = g_0(\varphi_c) - \Omega^2 r(\varphi_c)\cos\varphi_c \qquad (3)$$

where $g_0(\varphi_c)=GM_S/r(\varphi_c)^2$ is the local gravity, G is the gravitational constant and M_S the mass of Saturn. $S(\lambda,\varphi,t)$ is the disturbance in the form of a surface perturbation which models the storm's convective source (λ is the longitude, and φ is the planetographic latitude, see e. g. Sanchez-Lavega, 2011).

Previous models of the storm onset (Sanchez-Lavega and Battaner, 1987; Hueso and Sánchez-Lavega, 2004) and a large number of models and observations, including electrical activity and water ice detection, of the 2010 GWS indicates that deep water moist convection is the source of the storm

(Fisher et al., 2011; Sánchez-Lavega et al., 2011, 2012; Sayanagi et al., 2013; Dyudina et al. (2013), Sromovsky et al. 2013). Convective storms are a source of energy due to latent heat release, mechanical buoyant energy release conveyed by high vertical velocities (Sánchez-Lavega et al, 2011; Hueso et al., 2004), and internal energy transport. Vertically transported mass diverged aloft under geostrophic adjustment, and potential vorticity conservation also contributed to generate a powerful anticyclonic circulation (García-Melendo et al., 2013). SW models are decoupled from thermodynamic processes such as water moist convection as in the 2010 GWS, but we can model its action on the atmosphere by a combined effect of mass and energy perturbations in the form of a surface elevation perturbation ($S(\lambda, \varphi, t)$ in (1)). A surface elevation perturbation supplies potential energy which is not completely radiated away by gravity waves in the presence of rapid rotation. Under geostrophic adjustment, part of the injected potential energy is kept as a water surface elevation, part is radiated away in the form of gravity waves, and part is transformed into kinetic energy which will interact with the ambient zonal circulation. Mass and energy are injected only in the upper layer, representing a simplified form of Saturn's weather layer, where the storm energy and mass are deposited interacting with the background zonal winds. The amount of kinetic energy injected introduced in the model depends on the amount of initial potential energy (bump size), therefore initial volume injection also controls the amount of injected energy. Energy and mass sinks are represented by introducing Rayleigh dissipation term, which controls the evolution of the total amount of mass and energy (potential and kinetic) injected in the model.

We used the following Gaussian-shaped pulse form for mass injection:

$$S(r,t) = A_0 e^{-\left(r-r_0(t)\right)^2/\sigma^2} \left(F\left(t\right) - F\left(t - t_{end}\right)\right). \quad (4)$$

In (4) r represents the position of a point in the horizontal domain, $r_0(t)$ is the position of the perturbation, and $F(t)$ is the Heaviside function defined as

$$F(t)=\begin{cases}1, & t\geq 0\\ 0, & t<0\end{cases}. \qquad (5)$$

Pulse injection is started at $t=0$ and stopped at t_{end}. A_0 is the amplitude of the Gaussian pulse, and σ controls de spatial decay rate of the pulse away from $r_0(t)$. The time dependence of $r_0(t)$ allows to move the injected storm in the zonal direction at any chosen speed according to the observed drift velocity of the GWS convective source. In the discrete horizontal domain it was implemented by injecting a mass pulse only when the centre of the pulse moved onto the next grid point. The form of the injected perturbation as described in (4) is not modified during simulations.

The set of equations in (1) does not include topography, just a flat bottom. For the one-layer model, we are interested in isolating the effects of zonal winds $U(y)$ from storm dynamics. In this case, during the disturbance development we assume that zonal winds are not affected by the storm and we impose them by their algebraic addition to the horizontal velocity produced by perturbation velocities u and υ. We let the perturbation quantities u, υ, and h to evolve freely, whereas the variables numerically computed are $(u+U(y))$, υ, and h. In this case it is possible to study the interaction between the perturbation and the zonal wind without introducing topography.

We also used a two-layer SW model, where the topography of the surface η of the upper layer, and that of the lower layer, are computed so that their meridional gradients and the zonal winds are in geostrophic balance. At the planet's equator geostrophy is lost because the Coriolis parameter is zero, but pressure can be integrated (represented by the gradient $d\eta/dy$), and obtain the meridional

variation of surface η by assuming that there is not meridional wind ($\upsilon = 0$), and that initially the zonal wind $U(y)$ is not time dependent,. Topography is then calculated as

$$\eta(y) = -\int \frac{f(y)}{g(y)} U(y) dy + \eta_0 \qquad (6)$$

where η_0 is an integration constant.

In the two-layer model, the dynamic pressures of upper layer (layer 1), and the lower layer (layer 2), are given by:

$$\begin{cases} P_1 = \rho_1 g \eta_1 \\ P_2 = \rho_1 g \eta_1 + (\rho_2 - \rho_1) g \eta_2 \end{cases} . \qquad (7)$$

where $\eta_1 = \eta_2$ if *U(y)* is the same in both layers. In our simulations we set $\rho_2 \sim 60\rho_1$ - $100\rho_1$, so that the lower layer is almost rigid emulating an abyssal bottom with persistent zonal winds beneath the weather layer. In Appendix 1 we give details on the model numerical schemes.

4. Results

We adopted for each GWS simulation the zonal wind profile at the outbreak latitude from the following sources: (a) For the 1960 we used the Voyager 1-2 profile (Sanchez-Lavega et al., 2000); (b) For the 2010 case the Cassini profile (Garcia-Melendo et al., 2011), being it, at high latitudes, similar to the Voyager 1-2 profiles; (c) For the 1990 GWS the choice is more uncertain in view of the previously commented difference between Voyager and Cassini Equatorial profiles so we tested both profiles.

297

298 **4.1 Equatorial event (GWS 1990)**

299

300 ***4.1.1 GWS onset***

301

302 Our SW simulations reproduce the initial stages of the storm and allow fixing the background
303 equatorial zonal jet profile. The initial stages were well reproduced when the Voyager 1-2 zonal wind
304 profile was used, but were unsatisfactory for the Cassini profile. Sensitivity tests of the GWS
305 morphology to the shape of the zonal wind profile show that an equatorial Voyager profile
306 reproduces the observations (Figure 3, panel A). This is an important outcome which strongly
307 suggests that at cloud top level, when the storm onset was observed, the equatorial jet's shape in 1990
308 was similar to that in 1980. Results are very sensitive to the latitude where the initial perturbation is
309 injected, the injected volume per unit time, and the zonal wind profile shape. We can reproduce the
310 initial observed tilted elliptical spot (Sánchez-Lavega et al., 1991, Beebe et al., 1992), only when the
311 perturbation is injected about +12º ± 1º. If the perturbation is introduced ± 3º off the previously
312 mentioned latitude, the disparity between the storm's drift speed and the background zonal flow
313 produces advection phenomena that deform the disturbance's onset. We found almost no difference
314 between the results yielded by the 1-layer model with imposed zonal winds, and the 2-layer zonal
315 wind model with two active layers when the Rossby barotropic equatorial deformation radius
316 $L_E = (c/\beta)^{1/2}$ (c is Kelvin's phase speed, and β is the meridional gradient of the planetary vorticity)
317 was the same for the upper active layer as panel B in Figure 3 shows. In the two-layer case, zonal
318 winds where the same for the weather and abyssal layers with no vertical shear.

319 **[Figure 3]**

320 Sensitivity of GWS expanding area, shape and expansion rate to volume injection are shown in
321 Figure 4. The observed properties of the GWS nucleus resemble those observed in the real storm if
322 the volume injection rate, normalised with respect to the active layer thickness H, rates over Φ =

~$2x10^9$ m^2 s^{-1}. Although injected volume values obtained by the SW models cannot be directly translated into the real storm, the result is pointing out that the storm's dynamics totally changes with Φ. In our model, when the injected volume is appropriate, a feature similar to the observed storm nucleus forms (Figure 5); part of the injected mass propagates southward and interacts with the peak of the equatorial jet forming equatorial Rossby waves. By tuning the layer depth *h*, or equivalently L_E, it is possible to control the phase velocity of the Rossby waves. For high values of L_E, the negative phase velocity is faster and waves move significantly slower than the perturbation, which appears as an elongated nucleus when looking at the passive tracer distribution or potential vorticity (PV) field. Albeit, we cannot determine the particular nature of the Rossby wave. Its phase speed relative to the background zonal winds does not match the classical dispersion relation:

$$\omega = -\frac{\beta k}{k^2 + (2n+1)\beta / c} \qquad (8)$$

derived from SW linear theory for any n, but the geopotential field is very similar to the symmetric Rossby waves produced by forcing as described by Matsuno (1966). In fact, this is the type of Rossby waves we obtain in numerical experiments performed with a uniform background wind field. The geopotential field and circulation is also similar to a solitary Rossby wave, showing two symmetrical high pressure centers on both sides of the equator with their respective anticyclonic circulation, and a strong westwards zonal circulation between them (Boyd, 1985).

When the volume rate of injection is too small (Figure 4, panel 2) disturbance growth is more or less lineal, and the main mechanism responsible for material dispersion is pure advection by zonal winds. At the point of injection the Coriolis force forms a small anticyclone, but the strong meridional wind shear of the equatorial jet quickly drags the divergent injected mass towards the west at the north and towards the east at the south, following the shape of the north flank of the jet. This is not what we see for the 1990 storm.

[Figure 5]

4.1.2 The planetary-scale disturbance

Numerical experiments produce a zonal expansion of the storm along the North and South flanks of the source (Figure 6). The simulations that best reproduce the observations occur for $L_E \leq 3500$ km, normalised volume injection rates over ~2×10^9 m^2 s^{-1}, an injection latitude about +12º, and a storm speed of 365 m s^{-1}. Sensitivity tests to changes in theses parameters show large deviations from observations.

[Figure 6]

In the case of the storm expansion on the north side, a minimum normalised volume injection rate is necessary, but the value of L_E and the injection latitude are critical to achieve zonal expansion on the north side of the storm for the Voyager zonal wind profile. For too deep active layers (H > 1000 m), simulations reproduce the storm onset during the first days when the perturbation is injected at +12º. After then, material expansion towards the north ceases. If the latitude injection is under ~ +10º, then there is no northward expansion at all except when forcing is introduced at higher latitudes. We can achieve northward expansion for H > 1000 m when forcing is introduced above +12º, but then simulations differ from observations.

The northern disturbance forms a wavy pattern which propagates at a velocity ~ 200 m s^{-1} (westward of the nucleus) at latitude ~ +17º similar to that reported by Sánchez-Lavega et al. (1991). This is an advection phenomenon due to the strong meridional shear of the equatorial jet between +5º and +22º. The disturbance encircles the planet, spanning a band between latitudes +12º and +22º. The wavy pattern seems regular at the beginning of its formation, with a wavelength λ ~ 10º, similar to that on HST images, particularly at 440 nm (Westphal et al, 1992). In the SW simulations, waves break and

finally display a turbulent behaviour as they evolve remembering the behaviour of a classical Kelvin-Helmholtz instability (Vallis, 2006).

At the latitude of the storm source (+12°) and with the source moving at the observed initial velocity (365 m s^{-1}) simulations produce a gravity-Rossby wave that grows eastward of the nucleus, trapped around the Equator (Figure 6). In our simulations, the injected material leaves the southern flank of the nucleus (Rossby wave). Due to the β effect, the advected parcels conserving PV acquire negative relative vorticity and migrate northwards reaching a latitude limit between +7º and +10º, generating an oscillatory pattern between latitudes +10º and -10º with the crests and troughs separated by ~30º.forming a trapped planetary wave which encircles the simulation domain around the equator.

A part of the injected potential energy is radiated in the form of gravity waves being reflected at the northern and southern boundaries of the domain, then interacting with each other and the perturbation. These waves have not been observed and result in noise, so to analyse their importance in the results we did different tests in channels with meridional extents of ±50º, ±40º, and ±30º. We conclude that interactions of gravity waves with the storm are negligible. These gravity waves have much smaller amplitudes than the perturbation, on the order of ~100 to ~1000, so they transport little energy and do not modify the simulated storm. Figure 7 illustrates this result, which is also valid for 2010 and 1960 GWS simulations.

[Figure 7]

4.2 The mid-latitude event (GWS 2010)

The abundant high resolution data for the 2010 GWS (Section 2 and references therein) is a good test to check how well the SW model performs for such a storm. Numerical simulations of the storm head dynamics using the EPIC code were presented in Sanchez-Lavega et al. (2011) and García-Melendo et al. (2013). They serve as a control test to our present work. Most of our SW simulations were run

399 with an average horizontal resolution of 0.125 deg pix^{-1}, which is about twice as much as that for the
400 1990 GWS simulations. We obtained the best simulation results for small Rossby deformation radii
401 ($L_R = c/f$) (300 km $\leq L_R \leq$ 1000 km). For large L_R, the model turned out unstable with the production
402 of big vortices (Showman, 2007). It was possible to reproduce the onset and disturbance growth if the
403 mass source is located within a small range of latitudes between +37º and +38º (Figure 8). To
404 reproduce the storm, the injected normalised volume flux was $\Phi \sim 10^8$ m^2 s^{-1} compared to $\Phi \sim 10^9$ m^2
405 s^{-1} for the 1990 case. As a result, the injected mass rate needed to reproduce the storm was an order of
406 magnitude smaller than the 1990 event. A first comparison between the storm's cloud evolution and
407 the simulated PV maps show a striking resemblance. Most observed phenomena are reproduced by
408 the SW model, including the formation of one or several long-lived vortices at the end of the tail of
409 the storm, chains of small vortices and strong turbulence to the south of the storm between +36º and
410 ~ +28º due to the meridional wind shear of the north flank of the equatorial jet forming the storm's
411 south branch, and the generation of a north branch northwards +39º. The cloud front or "head" is also
412 reproduced including the structure of long open anticyclones forming the tail between the head and
413 the long-lived vortex (Dyudina et al., 2013; García-Melendo et al., 2013).
414
415 **[Figure 8]**
416
417 Storm's head dynamics is complex but it is captured by our simulations in its essentials (Figure 9).
418 García-Melendo et al. (2013) found that the storm's head had a high velocity rim, especially on its
419 north side, with winds up to 160 m s^{-1}. Mass injection and its interaction with the background zonal
420 wind generate a high pressure region with a strong radial gradient giving rise to a cloud front and the
421 high velocity rim around it due to potential energy conversion into kinetic energy after geostrophic
422 adjustment and interaction with zonal winds. The model tells us that there is upwelling of enormous
423 amounts of mass and energy. This result is consistent with EPIC simulations of the storm head

(García-Melendo et al., 2013). Dyudina et al. (2013) also argued, by invoking PV conservation, that the convective upwelling of mass must also transport negative vorticity.

[Figure 9]

Sayanagi et al. (2013) observed that the local zonal wind speed around the 2010 outbreak latitude had changed by as much as 40 m s^{-1}. We retrieved the zonal wind profile of the region by using automatic cross-correlation techniques between albedo scans extracted from Cassini ISS image pairs five months after the storm's demise (for a description of the retrieving technique see García-Melendo et al., 2011). We found that zonal wind speed changes were still persistent. Figure 10 shows how the zonal wind profile is affected by the injection of vorticity according to our simulations. The change is qualitatively similar to that measured in real images, confirming that relative vorticity injection as proposed by Sayanagi et al. (2013) may alter zonal wind speed.

[Figure 10]

4.3 The sub-polar event (GWS 1960)

There is very little information on the 1960 great storm (Figure 1). We do not exactly know when the onset took place, and how it evolved to the planetary scale disturbance observed for the first time in 1960 (Dollfus, 1960; Sánchez-Lavega, 2004). Nevertheless, its subpolar location where f is stronger than at any other latitude where giant storms have been observed, may give us important clues about the role played by Coriolis force on storm's dynamics. As mentioned in section 2, the 4 m s^{-1} drift reported for the storm by Dollfus (1960) and Sanchez-Lavega (1982) is probably that of a vortex formed after the onset, but not of the convective source.

449 We performed several numerical experiments by injecting mass between the +50º and +60º latitudes,
450 for L_R ~ 300 km. The actual speed of the convective source is also unknown, but following the
451 observed properties of the 2010 GWS, we moved the perturbation 15 ms^{-1} faster than the local zonal
452 wind except where the flow is westwards (~ +56º), and then the disturbance is moved -15 ms^{-1} faster
453 to the West. The injected mass flux is $\Phi \sim 10^8$ m^2 s^{-1} compared to $\Phi \sim 10^9$ m^2 s^{-1} and $\Phi \sim 10^8$ m^2 s^{-1}
454 for the 1990 and 2010 cases. When the perturbation was injected inside the ambient anticyclonic
455 region (latitude range from +56º to +60º), we obtained compact anticyclonic vortices or anticyclonic
456 cells which expanded slowly as more mass was injected that remember the observed ones (Dollfus,
457 1960). On the other hand, when the perturbation was injected close to or within a cyclonic region
458 (latitude range from +50º to +56º) there was a rapid expansion of the storm which quickly encircled
459 the whole simulation domain. Results are summarized in Figure 11.
460
461 **[Figure 11]**
462
463 We explain this storm's behaviour as follows. As commented by Dyudina et al. (2013) the storm
464 injects net anticyclonic relative vorticity. Our SW model also injects anticyclonic relative vorticity
465 when adding mass in presence of rotation due to geostrophic adjustment. If the anticyclonic injected
466 vorticity is within an anticyclonic region, it will form a stable vortex. If the background flow has
467 opposite relative vorticity, then the introduced mass will be sheared apart very quickly dispersing it
468 (Vasavada and Showman, 2005). Our simulations suggest that, in order to quickly expand the
469 perturbation around the planet, we must inject the perturbation between +56º and +54º, this is
470 coincident with the peak of a westwards jet. In this latitude range material is not only dispersed, but
471 also big compact vortices form. This mechanism also explains the dynamics of the 2010 GWS. It
472 appeared closed to a cyclonic region ~ +40º on a westwards jet peak. Part of the material exposed to
473 the cyclonic region quickly dispersed to the south, while the rest formed compact anticyclonic cells.
474

5 Summary and conclusions

In this work we have shown that forced SW models, under appropriate conditions, are able to reproduce the morphology of Saturn's giant storms "Great White Spots" that have been observed at different latitudes under different background zonal winds. These experiments give us insight in some of the most important dynamical phenomena involved in each case. Our main conclusions are summarized as follows:

Onset: The GWS model needs to be forced by a source, here represented by a Gaussian function which continuously injects material at a given rate. A fundamental result is that to reproduce the morphology and some of its most important dynamics, the source must be at a specific latitude, i.e. a specific point of the zonal wind profile, only for the right combination of L_R or L_E and injected volume per unit time we obtain the adequate response from the system. Furthermore, we cannot give real figures for the amount of injected mass, but we can compare the simulated 1990 and 2010 storms where in both cases L_E *i*s similar. For the 1960 storm, data is too uncertain to include it in the comparison. Successful simulations for the other two storms required injected volume rates of ~10^{12} m^3 s^{-1} and ~10^{11} m^3 s^{-1} for the 1990 and 2010 GWS respectively. As a result, the injected mass rate needed to reproduce the 1990 storm onset was an order of magnitude larger than the 2010 event.

Development: The interaction of this source with the background zonal wind profile defines the GWS evolution. Advection of the injected material is accompanied by different types of instability during the growing phase to a planetary-scale disturbance. Depending on latitude, the action of Coriolis force becomes very important in defining the kind of produced disturbance. Our SW models cannot account for real changes in the equatorial jet, because mass injection and dissipation are introduced in order to reproduce cloud top level morphology and to avoid a continuous increase of kinetic energy in the model that would lead to a continuous increase of the equatorial jet's intensity.

2010 GWS: The SW model reproduces the main characteristic of this event: an arc shaped front head with high peripheral velocity, cyclonic and anticyclone vortex series to the north and south of the head

source, a single long-lived anticyclone, etc. We think the success of our model rests in the way the perturbation is modeled. High resolution observations at different wavelengths of the 2010 event suggest that unperturbed air at the upper troposphere was continuously replaced with new material carrying fresh water and ammonia ice particles (Sromowsky et al, 2014). These observations support the moist convective origin for these events (Sanchez-Lavega and Battaner, 1987; Hueso and Sanchez-Lavega, 2004). Strong mass convection also conveys energy through latent heat release and mechanical energy due to the buoyant motion of air parcels. One of the consequences of convection aloft is vigorous divergence of new material at the cloud top level, which under rapid rotation adjusts to produce strong anticyclonic circulation. Our model operates in a similar simplified way, where mass is continuously deposited at the weather layer moving at its own velocity, but also releasing kinetic energy during geostrophic adjustment. Simulated fluid parcels acquire kinetic energy and interact with the background zonal winds producing the same kind of strong anticyclonic circulation observed in the real storm (García-Melendo et al., 2013). We must keep in mind ours is a simplified model where in all cases the perturbation source was kept constant. We believe real storms did not have a constant activity (in any of the events), but in front of this lack of information, we think a constant perturbation is a good first approximation to study its most relevant dynamical effects.

1990 GWS: Our numerical experiments strongly suggest that Saturn's equatorial jet, just before the 1990 GWS onset, was similar to the Voyager era profile. This most probably implies that little changes, if any, occurred in the wind profile between 1980 and 1990. The SW simulations indicate that the dynamics of the storm involves the generation of equatorial Rossby waves. Simulations reproduce the onset, smaller scale wave phenomena centred at +17º, and the large scale periodic phenomena detected near the equator. The northern development of the disturbance seems to involve a Kelvin-Helmholtz instability produced by the advection of material from the storm source in a meridional wind sheared profile.

1960 GWS: We can reproduce the quick expansion of the storm due to the dispersion of negative relative vorticity only by injecting mass near or at a cyclonic region at latitudes below +56º.

Simulations put an upper limit to the outbreak latitude and suggest that the big bright spot reported by Dollfus (1963) was actually a vortex that drifted at a different speed from the real convective source. If negative vorticity is injected by the storm, its general behaviour will strongly depend on the point on the zonal wind profile where it is injected. Our model predicts that convective material injected in anticyclonic regions will produce compact vortices or larger anticyclonic regions, and it will be quickly dispersed if it is in a cyclonic flank. This phenomenon was already known from many previous numerical experiments when studying Jovian vortices in an atmosphere with strong meridional shear (e.g. Achterberg and Ingersoll, 1994; Showman, 2007), but not related to giant Saturn's storms. This result reinforces the idea, again, of big convective events with updrafts of expanding air injecting big amounts of negative relative vorticity, big enough to even affect zonal wind measurements at cloud top level.

More modelling of giant Saturn's storms with higher resolution and more complex GCM models, including mass injection, convection and latent heat release at a planetary scale in realistic model atmospheres still remains as a path to obtain more details on their dynamics and its possible effects on the general circulation, including the generation of planetary waves.

Acknowledgments

This work was supported by the Spanish project AYA2012-36666 with FEDER support, Grupos Gobierno Vasco IT-765-13 and by Universidad del País Vasco UPV/EHU through program UFI11/55.

549 **Appendix 1: Numerical schemes**

550

551 We discretized the horizontal domain by using a staggered C-grid devised by Arakawa and Lamb
552 (1977). Once resolution is fixed in the longitudinal direction, we compute the number of grid points
553 in the meridional direction to obtain the same resolution at the centre of the domain, therefore
554 preserving as much as possible homogeneous resolution in the horizontal directions, which is
555 important when approaching the pole (see e.g. Morales-Juberías et al., 2011). The integration domain
556 corresponds to a channel with periodic boundary conditions in the *x* direction and with fully slip
557 impermeable rigid walls at the latitude limits. In the case of the active two-layered model, water
558 surface elevations were computed from bottom to top as

559

560 $$\frac{\partial \eta_1}{\partial t} = -\nabla \bullet \left(h\vec{u} \right) - \frac{h - h_0}{\tau_R} + \frac{\partial \eta_2}{\partial t} + S \,. \qquad \text{(A.1)}$$

561

562 where *S* is the surface disturbance, and τ_R is the Rayleigh time constant. One strategy for selecting a
563 specific τ_R, is to avoid a continuous increase of zonal wind kinetic energy when it is free to evolve in
564 the two-layer model, specially for the 1990 storm. A convenient τ_R was ~ 10^6 s. We used different
565 numerical schemes for different parts of the equation. The time integration of the horizontal
566 velocities *u*, υ, and water layer thickness η was performed by using a third-order Adams-Bashford
567 scheme (Durran, 1991). Dowling et al. (1998) commented its advantages before other popular single
568 step schemes in terms of stability or numerical dissipation, where current time derivatives are
569 computed as a linear combination of the previous ones as reproduced from expression (17) in
570 Dowling et al., for any variable ϕ as

571

572 $$\phi[t + \Delta t] = \phi[t] + \frac{\Delta t}{12}\left(23\frac{\partial \phi}{\partial t}[t] - 16\frac{\partial \phi}{\partial t}[t - \Delta t] + 5\frac{\partial \phi}{\partial t}[t - 2\Delta t] \right), \qquad \text{(A.2)}$$

where derivatives for times t, $t-\Delta T$, and $t-2\Delta t$ are from previous computed values. Time iterations are initialized for $t=\Delta T$, and $t=2\Delta T$ by using a first-order (identical to an Euler scheme), and second-order Adams-Bashford schemes respectively.

Advection was computed according to the flux form representation

$$\frac{Du}{Dt} = \frac{\partial u}{\partial t} + \frac{\partial (uu)}{\partial x} + \frac{\partial (uv)}{\partial y} - u\left(\frac{\partial u}{\partial x} + \frac{\partial v}{\partial y}\right), \qquad \text{(A.3)}$$

to be able to include a flux limiter function and therefore include a second order, non-oscillatory monotonicity-preserving upwind scheme. In this case we chose a Superbee Total Variation Diminishing (TVD) scheme (Harten, 1983; Fringer et al., 2005, and see Versteeg and Malalasakera (2007) for a general introduction to flux limiter schemes). It preserves very well sharp gradients (Trac and Pen, 2003) as for example the sharp pressure gradient encountered in the 2010 GWS around the convective source (García-Melendo et al., et al., 2013) without producing overshooting in the numerical solution due to the Gibbs effect. In the case of the mass conservation equation, which can be expressed in a pure flux form, finite volume TVD schemes can be readily applied. For this equation, mass fluxes in the C-staggered grid were naturally computed in each finite volume cell from the horizontal velocities at each cell-boundary, by first determining the sign of the velocity associated to every incoming flux, and therefore deciding which grid element was advected through the cell walls (Versteeg and Malasakera, 2007). To implement the evolution of the Coriolis term, we used a traditional semi-implicit scheme. To test our SW model we performed several classical tests which are described in Appendix B.

In our simulations we have the following free parameters: channel dimensions, space resolution, zonal wind profile, and active layer depth which in turn fixes the Rossby deformation radius

598 $L_R = \sqrt{gH}\,/\,f$ for midlatitudes, and the equatorial Rossby radius of deformation $L_E = \left\{\sqrt{gH}\,/\,\beta\right\}^{1/2}$,

599 where β is the planetary vorticity gradient and H is the layer thickness. Regarding the perturbation,

600 the free parameter is its intensity (units $m^3\ s^{-1}$) which is given by expression (4) through pulse

601 amplitude A_0, σ, and its maximum diameter $r = r_{\max}$, and by modifying the pulse injection rate. We

602 fix the pulse velocity as constant and zonal. Therefore, the coordinates for reference position $r_0(t)$ in

603 the channel are $(u_0 t + x_0, y_0)$, where u_0 is the pulse zonal speed, and x_0 and y_0 are constant values that

604 give the perturbation's initial position. At the location $r_0(t)$, a totally passive tracer or dye was

605 injected with every pulse. At the same time, tracer advection by the total velocity field $(u + U(y), \upsilon)$

606 was recomputed every time step, out of the injection region, after updating the perturbation velocities

607 as

608

609 $$\frac{DT_c}{Dt} = \frac{\partial T_c}{\partial t} + \frac{\partial (uT_c)}{\partial x} + \frac{\partial (vT_c)}{\partial y} - T_c\left(\frac{\partial u}{\partial x} + \frac{\partial v}{\partial y}\right) = 0\,.$$

610

611 where T_c represents tracer concentration. A passive dye is useful to visually isolate the evolution of

612 the storm, as in the real storm injected bright clouds do at the visible cloud level. Since PV is

613 conserved by fluid parcels, storm evolution in the PV field is in most cases identical to that given by

614 tracer evolution. We arbitrarily adopted a tracer concentration of 1 for the injected dye, which could

615 drop to 0 when advection dilutes it completely.

616

617 Grid resolution ranged between 0.25 deg pix^{-1} and 0.125 deg pix^{-1}, allowing us to reproduce most of

618 the important morphological and dynamical details of the GWSs. This spatial resolution fixed the

619 time step between 5s and 60s to preserve numerical stability and consistency. For the equatorial

620 storm, most of the simulations were performed at a longitudinal resolution of 0.25 deg pix^{-1} (~260

621 km pix^{-1}). Under the presence of geostrophic balance and for equatorial simulations, we used short

622 time steps (5 s to 10 s) for the two-layer models to avoid a significant damping of the equatorial jet as
623 illustrated by test results described in Appendix 2. Table A.1 summarizes the range of parameters
624 adopted for the 1960, 1990, and 2010 GWSs.
625
626 **[Table A.1]**
627
628 **Appendix 2: Model Validation**
629 To test our SW model, we performed some of the classical tests proposed by Williamson et al.
630 (1992). These tests are devised for one-layer SW global circulation models (GCM) on the sphere, but
631 our model, although works in spherical coordinates, is run on a channel and no solution over the
632 poles is implemented. So we performed those tests which could be run in a channel without including
633 the pole. We tested advection of a cosine bell on the equator (test 1) for the case, $\alpha=0$ in expressions
634 (75) and (76) in Williamson et al. to keep the velocity field nondivergent; global steady state
635 nonlinear zonal geostrophic flow for a jet on the equator (test 2, $\alpha=0$ with), which also was a good
636 test to check the stability of our two-layer simulations where the Saturn's equatorial jet was free to
637 evolve in the storm after initialization using geostrophic balance; steady state nonlinear zonal
638 geostrophic flow with compact support for a jet centered at midlatitudes (test 3), with zero velocity at
639 the latitudinal boundaries of the channel, and finally we simulated a Rossby-Haurwitz wave between
640 the ±80º latitude limits (test 6). Our results indicate that our model performs well in all these cases.
641 Figure A.1 shows simulations in a 360-degree long channel between 40ºS and 40ºN latitudes for
642 256x114, 512x228, and 1024x556 point grid resolutions after the cosine bell has been advected for
643 12 days (a complete revolution along the equator). Figure A.2 displays total errors, and show that the
644 TVD scheme should work very well in the 2010 GWS case, where there are relatively sharp gradients
645 of the prognostic variables. Error also diminishes with increasing grid resolution which proves the
646 consistency of the model.
647

[Figure A.1, Figure A.2]

Figure A.3 shows the results of geostrophic equilibrium for a jet on the equator, not after 12 days as suggested by Williamson et al. (1992), but for 50 day simulations, at different grid resolutions and time steps, according to their (90) to (95) expressions adapted to a 60ºS to 60ºN channel. Results show that the model is fully consistent and did an excellent job with decreasing errors for increasing grid resolution and decreasing time steps, with solutions converging to the jet model. In Figure A.3 we only represent the height field because the results for the zonal velocity field are similar.

[Figure A.3]

Test 3 in Williamson et al., with a zonal jet centered at midlatitudes (+30º) is a more demanding one, but Figure A.4 shows that our model is also fully consistent, as it converges by keeping the initial configuration by decreasing space and time steps.

[Figure A.4]

Finally, Figure A.5 shows results for the simulation of a Rossby-Haurwitz wave, which also shows the consistency of the model. We therefore can be confident that our numerical scheme is not introducing important artefacts and that we can draw conclusions within the frame of a SW model.

[Figure A.5]

671 **References**

672

673 Acarreta, J. R. and A. Sánchez-Lavega, 1999: Vertical Cloud Structure in Saturn's 1990 Equatorial
674 Storm, *Icarus*, **137**, 24-33, doi: 10.1006/icar.1998.6034.

675

676 Achterberg, R. K., and A. P. Ingersoll, 1994: Numerical-simulation of baroclinic Jovian vortices, *J.*
677 *Atmos. Sci.*, **51**, 541–62, doi: 10.1175/1520-0469(1994)051<0541:NSOBJV>2.0.CO;2.

678

679 Arakawa, A., and V. Lamb, 1977: Computational design of the basic dynamical processes of the
680 UCLA General Circulation Model. *Methods Comput. Phys.*, **17**, 173–265.

681

682 Archinal, B. A. M. A'Hearn, et al., Report of the IAU/IAG working group on cartographic
683 coordinates and rotational elements: 2009. ***Celestial Mech. Dyn. Astron.* 109**, 101-135 (2010).

684

685 Barnet, C. D., Westphal, J. A., Beebe, R. F., and L. F. Huber, 1992: Hubble Space Telescope
686 Observations of the 1990 Equatorial Disturbance on Saturn: Zonal Wunds and Central Meridian
687 Albedos, *Icarus*, **100**, 499-511, doi: 10.1016/0019-1035(92)90113-L.

688

689 Beebe, R. F., Barbet, C., Sada, P. V., and A. S. Murrell, 1992: The Onset and Growth of the 1990
690 Equatorial Disturbance on Saturn. *Icarus*, **95**, 163-172, doi: 10.1016/0019-1035(92)90035-6.

691

692 Boyd, J. P., 1985: Equatorial Solitary Waves. Part 3: Westward-Traveling Modons, *J. Phys.*
693 *Oceanogr.*, **15**, doi: 10.1175/1520-0485(1985)015<0046:ESWPWT>2.0.CO;2.

694

695 Cushman-Roisin, B., and Beckers, J-M, 2011: Introduction to Geophysical Fluid Dynamics,
696 Academic Press; 2 edition.

Dowling, T.E., Fischer, A.S., Gierasch, P.J., Harrington, J., Lebeau, R.P., and Santori, C.M., 1998: The Explicit Planetary Isentropic-Coordinate (EPIC) atmospheric model. *Icarus*, **132**, 221–238, doi: 10.1006/icar.1998.5917.

Dollfus, A., 1963: Mouvements Dans L'Atmosphère de Saturne en 1960. Observations coordonnées per l'Union Astronomique Internationale, *Icarus*, **2**, 109-114, doi: 10.1016/0019-1035(63)90010-1.

Durran, D. R. 1991: The third-order Adams–Bashforth method: An attractive alternative to leapfrog time differencing, *Mon. Weather Rev.*, **119**, 702–720.

Dyudina, U. A., Ingersoll, A. P., Ewald, S. P., Porco, C. C., Fischer, G., and Y. Yair, 2013: Saturn's visible lightning, its radio emissions, and the structure of the 2009–2011 lightning storms, *Icarus*, **226**, 1021-1037, doi: 10.1016/j.icarus.2013.07.013.

Fischer, G., and Coauthors, 2011: A giant thunderstorm on Saturn, *Nature*, **475**, 75-77, doi: 10.1038/nature10205.

Fletcher, L. N., and Coauthors, 2011: Thermal Structure and Dynamics of Saturn's Northern Springtime Disturbance, *Science*, **332**, 1413-1417, doi: 10.1126/science.1204774.

Fletcher, L. N., and Coauthors, 2012, The origin and evolution of Saturn's 2011–2012 stratospheric vortex, *Icarus*, **221**, 560–586, doi: http://dx.doi.org/10.1016/j.icarus.2012.08.024

Fringer, O. B., Armfield, S. W., and R. L. Street, 2005: Reducing numerical diffusion in interfacial gravity wave simulations, *Int. J. Numer. Methods Fluids*, **49**, 301-329, doi: 10.1002/fld.993.

García-Melendo, E., Pérez-Hoyos, S., Sánchez-Lavega, A., Hueso, R., 2011: Saturn's zonal wind profile in 2004–2009 from Cassini ISS images and its long-term variability, *Icarus*, **215**, 62-74, doi: 10.1016/j.icarus.2011.07.005.

García-Melendo, E., Hueso, E., Sánchez-Lavega, A., Legarreta, J., del Río-Gaztelurrutia, T., Pérez-Hoyos, S., and J. F. Sanz-Requena, 2013: Atmospheric dynamics of Saturn's 2010 giant storm, *Nat. Geosci.*, **6**, 525-529, doi: 10.1038/NGEO1860.

Gill, A. E., 1982: Atmosphere-Ocean Dynamics, Academic Press, 662.

Harten, A., 1983: High resolution schemes for hyperbolic conservation laws, *J. Comput. Phys.*, **49**, 357-393, doi: 10.1016/0021-9991(83)90136-5.

Hubbard, W. B., M. Dougherty, D. Gautier, and R. Jacobson, 2009: The Interior of Saturn, in Saturn from Cassini-Huygens, Dougherty, L. W. Esposito, S. M. Krimigis (eds.), Springer (2009).

Hueso, R., and A. Sánchez-Lavega, 2004: A three-dimensional model of moist convection for the giant planets II: Saturn's water and ammonia moist convective storms, *Icarus*, **172**, 255-271, doi: 10.1016/j.icarus.2004.06.010.

Ingersoll, A.P., Beebe, R.F., Conrath, B.J., and G. E. Hunt, 1984: Structure and dynamics of Saturn's atmosphere. *Saturn*, Gehrels, T., and M. S. Matthews, Univ. Of Arizona Press, 195–238.

747 Laraia, A. L., A.P. Ingersoll, M.A. Janssen, S. Gulkis, F. Oyafuso, and M. Allison, 2013: Analysis of
748 Saturn's thermal emission at 2.2-cm wavelength: Spatial distribution of ammonia vapour, *Icarus*,
749 **226**, 641-654, doi: 10.1016/j.icarus.2013.06.017.
750
751 Matsuno, T., 1966: Quasi-Geostrophic Motions in the Equatorial Area. *J. Meteor. Soc. Japan*, **44**, 25-
752 43.
753
754 Morales-Juberías, R., Sayanagi, K. M., Dowling, T. E., and A. P. Ingersoll, 2011: Emergence of
755 polar-jet polygons from jet instabilities in a Saturn model. *Icarus*, **211**, 1284-1293, doi:
756 10.1016/j.icarus.2010.11.006.
757
758 Pérez-Hoyos, S., and A. Sánchez-Lavega, 2006: On the vertical wind shear of Saturn's equatorial jet
759 at cloud level. *Icarus*, **180**, 161–175, doi: 10.1016/j.icarus.2005.07.011.
760
761 Porco, C. C., and Coauthors, 2005: Cassini Imaging Science: Initial Results on Saturn's Atmosphere,
762 *Science*, **307**, 1243-1247, doi: 10.1126/science.1107691.
763
764 Sánchez-Lavega, A., 1982: Motions in Saturn's atmosphere - Observations before Voyager
765 encounters, *Icarus*, **49**, 1-16, doi: 10.1016/0019-1035(82)90052-5.
766
767 Sánchez-Lavega, A., and E. Battaner, 1987: The nature of Saturn's Great White Spots, *Astron.*
768 *Astrophys.*, **185**, 315-326.
769
770 Sánchez-Lavega, A., Colas, F., Lecacheux, J., Laques, P., Miyazaki, I., and D. Parker, 1991: The
771 Great White Spot and disturbances in Saturn's equatorial atmosphere during 1991, *Nature*, **353**, 397-
772 401, doi: 10.1038/353397a0.

773

774 Sánchez-Lavega, A., 1994: Saturn's Great White Spots. *CHAOS*, **4**, 341-353, doi: 10.1063/1.166012

775

776 Sánchez-Lavega, A., and Coauthors, 1996: Large-Scale Storms in Saturn's Atmosphere During 1994,

777 *Science*, **271**, 631-634, doi: 10.1126/science.271.5249.631.

778

779 Sánchez-Lavega, A., Rojas, J.F., and P. V. Sada, 2000: Saturn's zonal winds at cloud level, *Icarus*,

780 **147**, 405–420, doi: 10.1006/icar.2000.6449.

781

782 Sánchez-Lavega, A., Pérez-Hoyos, S., Rojas, J. F., Hueso, R. and R. G. French, 2003: A strong

783 decrease in Saturn's equatorial jet at cloud level, *Nature*, **423**, 623-625, doi: 10.1038/nature01653.

784

785 Sánchez-Lavega, A., Hueso, R., Pérez-Hoyos, S., Rojas , J. F., and R.G. French, 2004: Saturn's cloud

786 morphology and zonal winds before the Cassini encounter, *Icarus*, **170**, 519-523, doi:

787 10.1016/j.icarus.2004.05.002.

788

789 Sánchez-Lavega, A., 2011: An Introduction to Planetary Atmospheres, CRC Press, 629.

790

791 Sánchez-Lavega, A., and Coauthors, 2011: Deep winds beneath Saturn's upper clouds from a

792 seasonal long-lived planetary-scale storm, *Nature*, **475**, 71–74 doi: 10.1038/nature10203.

793

794 Sánchez-Lavega, A., and Coauthors, 2012: Ground-based observations of the long-term evolution

795 and death of Saturn's 2010 Great White Spot. *Icarus*, **220**, 561-576, doi:

796 10.1016/j.icarus.2012.05.033.

797

798 Sanz-Requena, J. F., Pérez-Hoyos, S., Sánchez-Lavega, A., del Río-Gaztelurrutia, T., Barrado-
799 Navascués, D., Colas, F., Lecacheux, J., and D. Parker, 2012: Cloud structure of Saturn's 2010 storm
800 from ground-based visual imaging, *Icarus*, **219**, 142-149, doi: 10.1016/j.icarus.2012.02.023.
801
802 Sayanagi, K. M. And A. P. Showman, 2007: Effects of a large convective storm on Saturn's
803 equatorial jet, *Icarus*, **287**, 520-539, doi: 10.1016/j.icarus.2006.10.020.
804
805 Sayanagi, K. M., Dyudina, U. A., Ewald, S. P., Fischer, P. G., Ingersoll, A. P., Kurth, W. S., Muro,
806 G. D., Porco, C. C., R. A. West, 2013: Dynamics of Saturn's great storm of 2010–2011 from Cassini
807 ISS and RPWS, *Icarus*, **223**, 460-478, doi: 10.1016/j.icarus.2012.12.013.
808
809 Seidelmann, P.K., and Coauthors, 2007: Report of the IAU/IAG working group on cartographic
810 coordinates and rotational elements: 2006, *Celestial Mech. Dyn. Astron.*, **98**, 155–180, doi:
811 10.1007/s10569-007-9072-y.
812
813 Showman, A., 2007: Numerical Simulations of Forced Shallow-Water Turbulence: Effects of Moist
814 Convection on the Large-Scale Circulation of Jupiter and Saturn, *J. Atmos. Sci.*, **64**, 3132-3157, doi:
815 10.1175/JAS4007.1.
816
817 Sromovsky, L. A., Baines, K. H., and P.M. Fry, 2013: Saturn's Great Storm of 2010–2011: Evidence
818 for ammonia and water ices from analysis of VIMS spectra, *Icarus*, **226**, 402-418, doi:
819 10.1016/j.icarus.2013.05.043.
820
821 Trac, H., and U. Pen, 2003: A Primer on Eulerian Computational Fluid Dynamics for Astrophysics,
822 *Publ. Astron. Soc. Pac.*, **115**, 303-321, doi: 10.1086/367747.
823

824 Vallis, G. K., 2006: Atmospheric and Ocean Fluid Dynamics, Cambridge University Press.
825
826 Vasavada, A. R., and A. P. Showman, 2005: Jovian atmospheric dynamics: an update after Galileo
827 and Cassini, *Rep. Prog. Phys.*, **68**, 1935–1996, doi: 10.1088/0034-4885/68/8/R06.
828
829 Versteeg, H., and Malasakera, W., 2007: An Introduction to Computational Fluid Dynamics: The
830 Finite Volume Method, Prentice Hall; 2 edition.
831
832 Westphal, J. A., Baum, W. A., Ingersoll, A. P., Barnet, C. D., De Jong, E. M., Danielson, G. E., and
833 J. Caldwell, 1992: Hubbe Space Telescope Observations of the 1990 Equatorial Disturbance on
834 Saturn: Images, Albedos, and Limb Darkening, *Icarus*, **100**, 485-498, doi: 10.1016/
835
836 Williamson, D. L., Drake, J. B., Hack, J. H., Jakob, R., and Swarztrauber, P. N., 1992: A Standard Test
837 Set for Numerical Approximations to the Shallow Water Equations in Spherical Geometry, *J. Comput.*
838 *Phys.*, **1992**, 221–22

Event	Affected latitude band	Head "bright spot"		Ambient vorticity $\zeta = \partial u / \partial y$ (s^{-1})	f (s^{-1})	β (m^{-1} s^{-1})
		Latitude	Velocity (m s^{-1})			
GWS 1960	48ºN – 60ºN [78ºN]*	57ºN ± 1º	4.0	2.2×10^{-6}	2.6×10^{-4}	3.6×10^{-12}
GWS 1990	15ºS – 25ºN	12ºN ± 1º [5ºN ±2º]†	365.0 [402.0]†	-3.7×10^{-5} [2.0×10^{-6}]†	5.5×10^{-5}	5.4×10^{-12}
GWS 2010	25ºN – 47ºN	40ºN ± 1º	-27.8	2.8×10^{-6}	1.8×10^{-4}	4.7×10^{-12}

Table 1. Summary of the observed properties for the studied events. *The 1960 GWS effects were initially confined to a latitude band between 48ºN and 60ºN, but a month after its discovery, it started to expand up to ~+80. †The onset of the 1990 storm took place at 12ºN, but after two weeks the activity source migrated equatorwards to +5º. In the last two columns, f and β are given for 12ºN.

Grid resolution (degrees pixel^{-1})	0.25 and 0.125
Number of layers	1, 2
Active layer thickness (m)	50 to 2000
Time step (s)	5 to 60
Zonal wind profiles	Voyager* and Cassini**
Density ratio between active and abyssal layer	60 and 100
Channel longitude	100º to 360º
Latitude intervals	[-40ºS,+40ºN]†, [+24ºN,+54ºN]††, [+40ºN,+70ºN]†††
τ_R (s)	10^5 to 10^9
Pulse amplitude (m)	5 to 500
Pulse σ (degrees)	3.5 to 800‡
Pulse radius (degrees)	1.5, 1.75, 2.0, 2.5
Pulse velocities (m s^{-1})	365 and 400†, -28††, [-20,+80]†††

Table A1. Parameter space used in SW simulations. * Sánchez-Lavega et al., 2000. ** García-Melendo et al., 2011. † 1990 GWS. †† 2010 GWS. ††† 1960 GWS. ‡ We used values > 100º to get a pulse cylindrical shape.

Figure captions

Figure 1. Morphology and evolution of the last three GWS events. (A) Drawing of the 1960 GWS as observed by Dollfus on 27 April 1960 on the 0.6 m telescope at Pic du Midi (adapted from Figure 1 in Dollfus, 1963); (B) Onset of the 1990 GWS observed with the 1-m telescope at Pic du Midi on 2 October 1990 in V (adapted from Figure 1 in Sánchez-Lavega et al., 1991); (C) Mature state of the 1990 GWS observed by the HST on 17 November 1990; (D) Cylindrical projection of the planetary-scale 1990 perturbation in its mature state in blue light (λ= 439 nm), as observed by the HST on 17 November 1990. At a 180º longitude and +3º, the convective source appears as a bright dot (adapted from Figure 2 in Westphal et al., 1992); (E) False colour Cassini images showing the morphology evolution of the 2010 GWS during ~4 months. Individual frames are a composition of the CB2 (750 nm), MT2 (727 nm), and MT3 (889 nm) (adapted from Figure 4 in Sayanagi et al., 2013); (F) High resolution Cassini image of the 2010 GWS one month later than the perturbation outbreak showing the fundamental storm's morphology: the storm front shaping the head at longitude ~ 110º, the long-lived anticyclonic vortex (bluish vortex at ~75º longitude), the tail or region in between with anticyclonic circulation, and the turbulent wake behind the long-lived vortex for longitudes smaller than 60º (adapted from Figure 5 in Sayanagi et al., 2013).

Figure 2. Saturn's zonal wind profile measured from Voyager images in 1980-81 (Sánchez-Lavega et al., 2000, red line). The pale blue section is a symmetric reconstruction used in simulations of the missing part of Voyager profile. The Cassini zonal wind profile is represented by the purple line (García-Melendo et al., 2011). Solid dots on the equatorial jet indicate the position and velocity of the 1990 GWS nuclei, while the 2010 and 1960 GWS perturbations appeared close to the +40º and +56º westward jets. The light green shadowed areas represent the regions disturbed by the storms.

Figure 3. (A) Tracer concentration maps (see explanation in Appendix 1 about tracer injection) of the evolution of the 1990 GWS onset as simulated by a 1-layer SW model after 5 days for L_E = 4300 km, and interpolated profiles between the Voyager and the Cassini era profiles. Tracer concentration is coded from arbitrary maximum values of 1.0 (white), to the black background (concentration = 0) and in all figures thereafter. Since PV is conserved, PV maps yield the same results than tracer concentration maps, but tracer concentration allows visually isolating the perturbation from the rest of the domain. Only the profiles close to Voyager's yield an onset evolution similar to the real storm. Numbers associate each simulation to its corresponding zonal wind profile. The solid dot on the superimposed profiles represents the 1990 GWS outbreak at +12º. (B) The top panel is a 1-layer SW simulation with a resolution of 262 km pix^{-1}, for L_E = 3900 km and Voyager era imposed winds. The bottom panel is the result of a geostrophically balanced 2-layer SW model by using the same Voyager wind profile with the same horizontal resolution and L_E for $\rho_2=60\rho_1$. Outcomes are after 5 days of simulation. No important differences can be appreciated between simulations.

Figure 4. Top-left panel: cloud area growth for two-layer simulations for perturbation injection rates from ~2x10^{11} m^3 s^{-1} to ~3.0x10^{12} m^3 s^{-1}. Blue lines are for those simulations which develop a nucleus during the first days, while red lines are for those simulations which do not develop it. Green lines show those cases where nuclei appear later than 3-4 days after perturbation injection is initiated. Top-right panel: cloud expansion rate is strongly correlated with the normalised volume injection rate with respect to layer thickness. Solid color corresponds to the same color code in top-left panel. Bottom panel: 1 and 2 are two tracer concentration map examples, after a simulation time of four days. The corresponding points on top-right panel are also marked. Simulation 1 is for L_E = 3100 km, and 2 for L_E = 2800

Figure 5. From top to bottom, development of the storm nucleus as an equatorial Rossby wave for a two-layer model the days 1, 3, 5, and 7. Left figures represent the active top layer depth including the perturbation circulation. Right panels represent the dispersion of a passive tracer for the same days. L_E = 3100 km. During the Rossby wave formation mass injection produces a divergent anticyclone that

injects mass at lower latitudes originating the wave. In the seventh day it is evident the rotation of the anticyclonic region below the equator.

Figure 6. Potential vorticity field of 1990 GWS expansion according to our SW simulation. A Kelvin-Helmholtz instability can be observed as a small scale wavy pattern expanding westward, and the gravity-Rossby wave expands eastward interacting with the nucleus. One-layer simulation with L_E = 3000 km.

Figure 7. Fluid surface elevation fields for the same simulation showed in Figure 6, where results have been highly contrasted to show gravity waves. Simulations are for a 1-layer flat-bottomed model, imposed winds, with L_E = 3000 km.

Figure 8. Simulated PV field for the 2010 GWS in a 240ºx30º channel with L_R = 350 km, a resolution of 0.125 deg pix^{-1}, and continuous mass injection of a perturbation moving at of -27.8 m s^{-1}, with respect to System III rotational frame.

Figure 9. Strong anticyclonic circulation of the storm's head as simulated by the SW model (right), and PV field (left) for the same simulation presented in Figure 10 for day 48. Compare it with Figure 3 in García-Melendo et al. (2013). The strong anticyclonic circulation has a magnitude similar to that detected in the real storm.

Figure 10. Zonal wind profile around the 40ºN westward jet retrieved from CB2 Cassini images taken in January 2012 (solid line), six months after the demise of the 2010 GWS, compared with the wind profile measured before the storm (grey line, García-Melendo et al., 2011), and the one obtained from SW simulations (dashed line).

Figure 11. PV maps of 1960 GWS simulations after 40 days for an injected perturbation at +57º (upper panel, $\Phi \sim 1.6 \times 10^8$ m^2 s^{-1}), +56º (middle panel, $\Phi \sim 4 \times 10^8$ m^2 s^{-1}), and +52º (bottom panel, Q ~ 4×10^8 m^2

s^{-1}). When the perturbation is injected in an anticyclonic flank (+57º) of the zonal wind profile, it forms a compact anticyclonic region.

Figure A.1. Longitudinal and meridional height field profiles for the cosine-bell advection case at the equator after one rotation along the Earth equator (12 days) as a function of grid resolution for a time step of 5s. Differences between the original function and the advected function decrease with increasing spatial resolution, especially in the meridional direction. For high spatial resolution the original function and the final advected one are indistinguishable.

Figure A.2. Errors obtained for the cosine-bell advection test after 12 days. They show a good behaviour of advection numerical schemes, with no overshooting errors.

Figure A.3. Dependence on grid resolution and time step for test 2, an equatorial jet in geostrophic equilibrium (from Williamson et al.,1992), in a simulation channel 360º long, spanning latitudes from -60º to +60º after 50 simulation days. Computations are made for 128x43, 256x86, and 512x172 grid points. Results show that the numerical scheme is completely consistent, since simulations converge towards the true jet by decreasing the time step.

Figure A.4. The same as Figure A.3 but for a jet centered at 30ºN after 50 days of simulation for a channel 360 degree-long between the 30ºS and 80ºN latitude for different grid resolutions and time steps. Left column represents the height field deviations at simulation day 50. Middle column represents the final height field compared with the initial one (solid black line). Right column represents zonal winds.

Figure A.5. Results for test 6 from Williamson et al. (1992) for a 12 day simulation. The model keeps a stable Rossby-Hurwitz wave for the simulation period.

Figure 1 (electronic version)

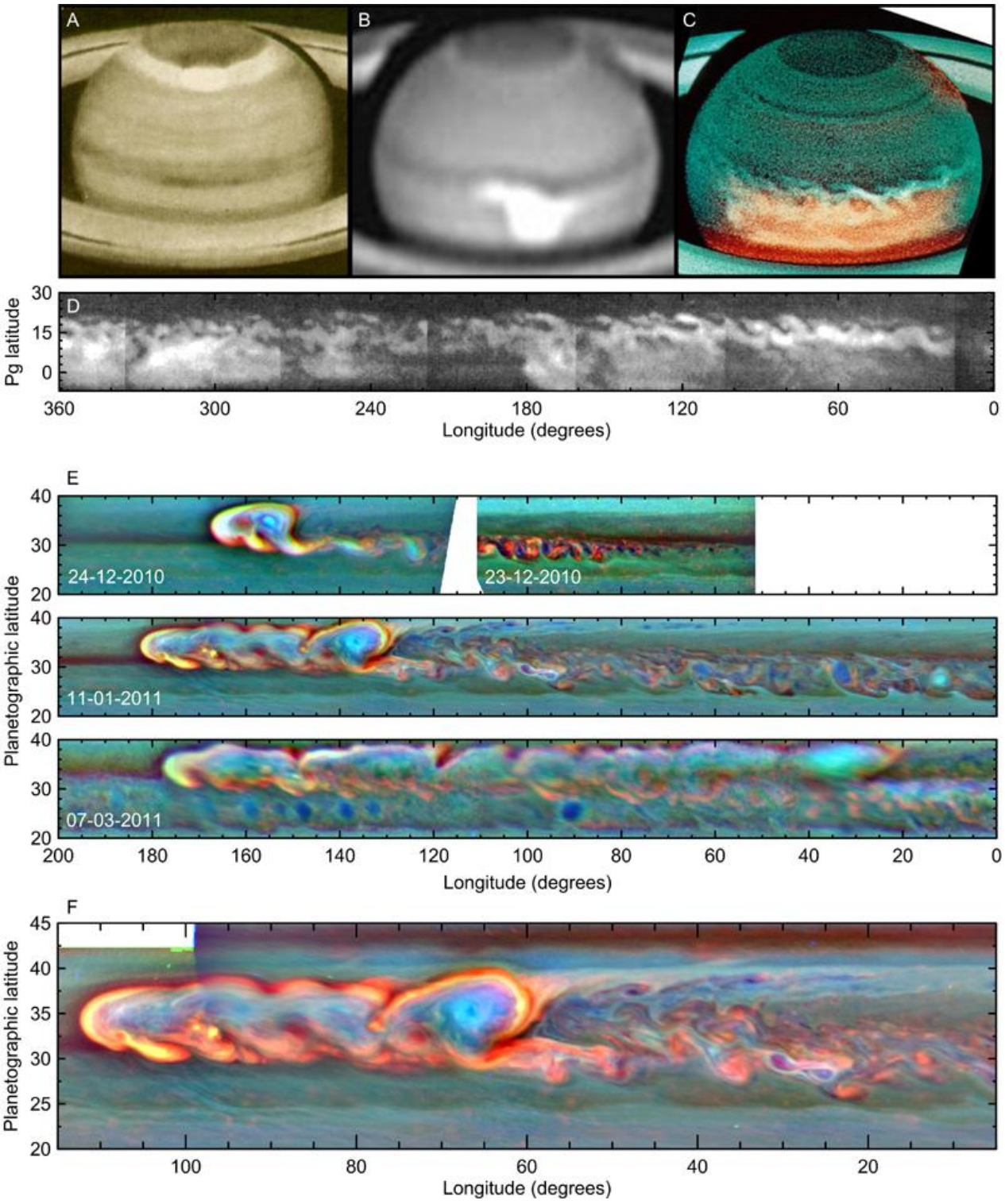

Figure 1 (printed version)

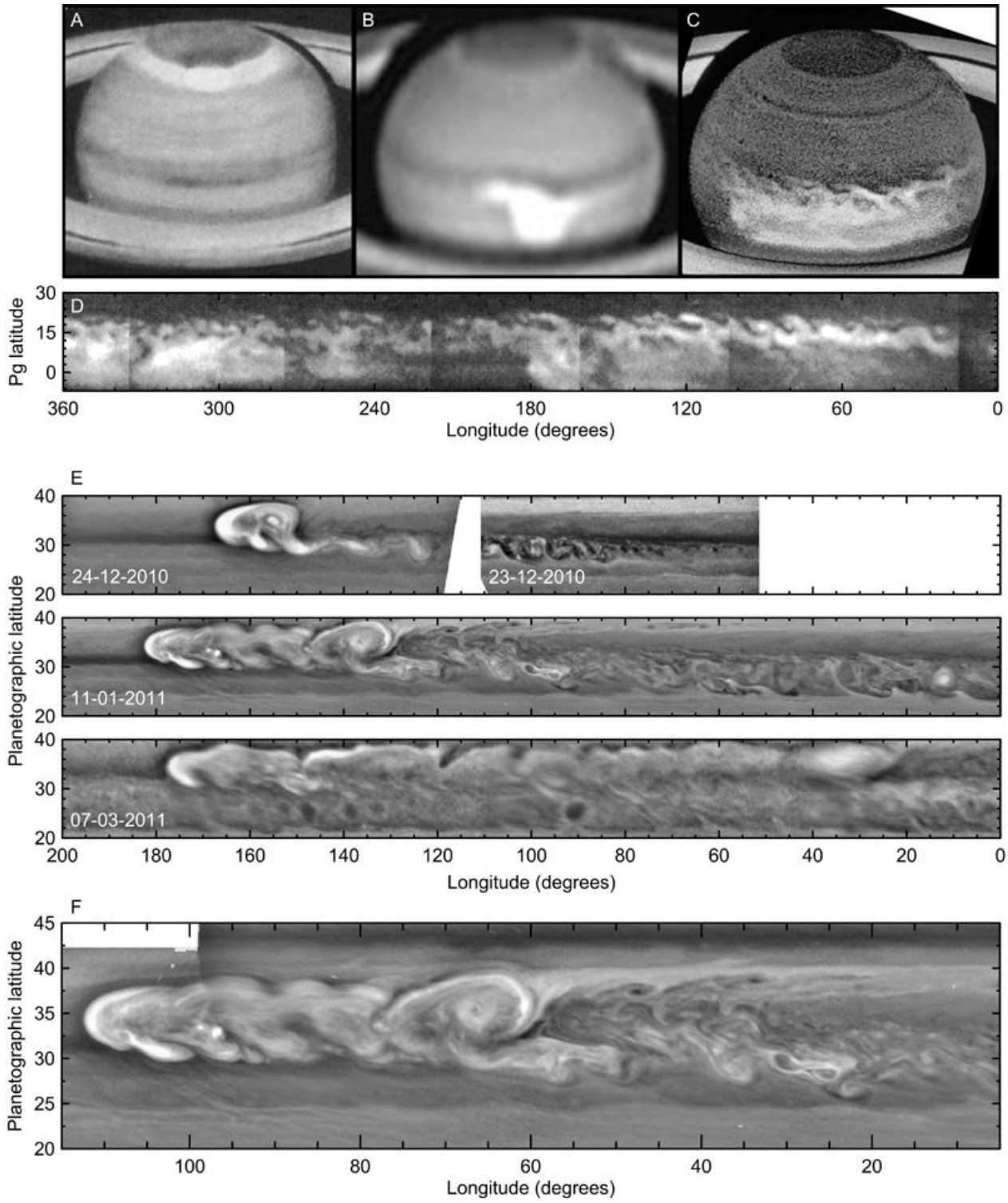

Figure 2 (electronic version)

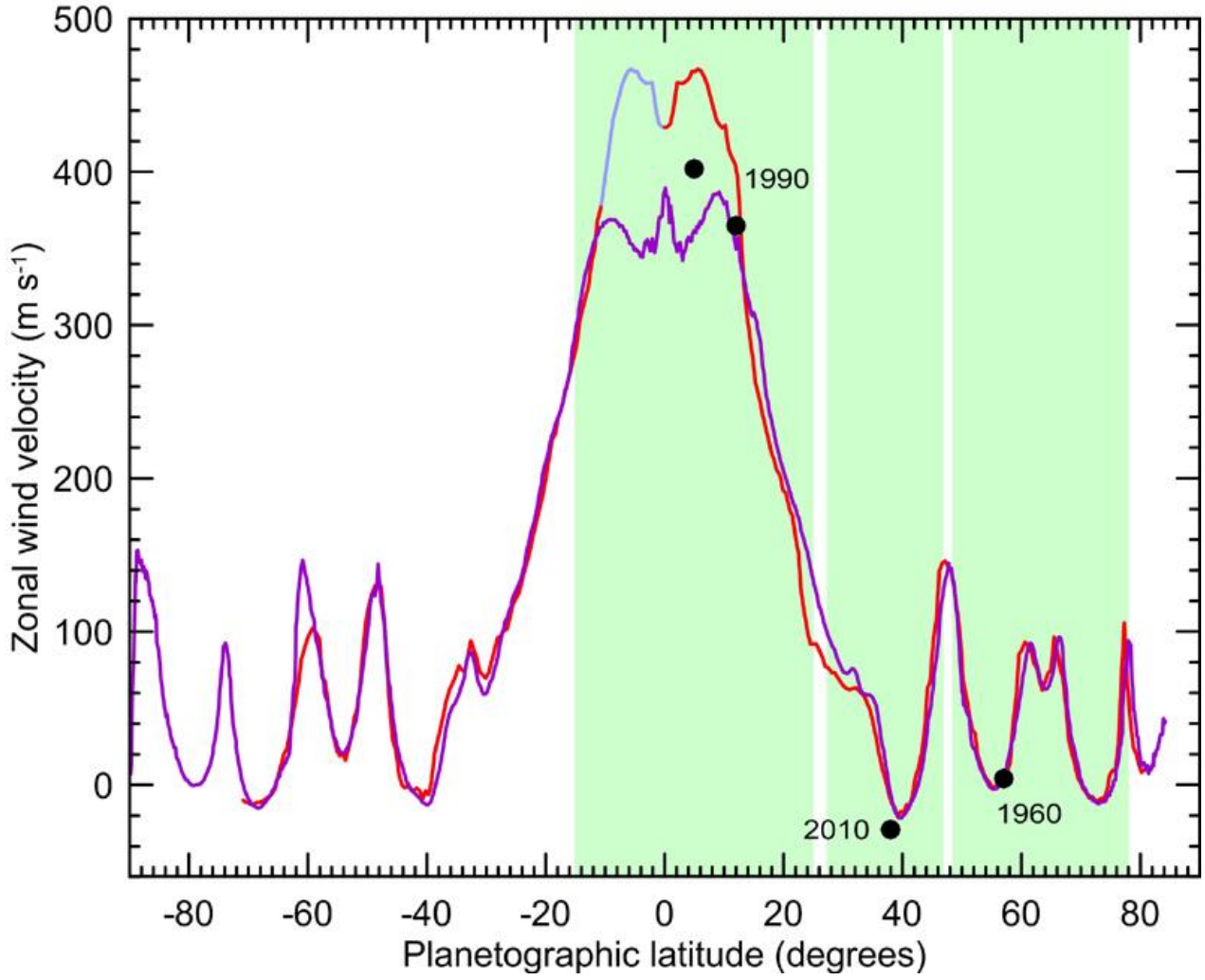

Figure 2 (printed version)

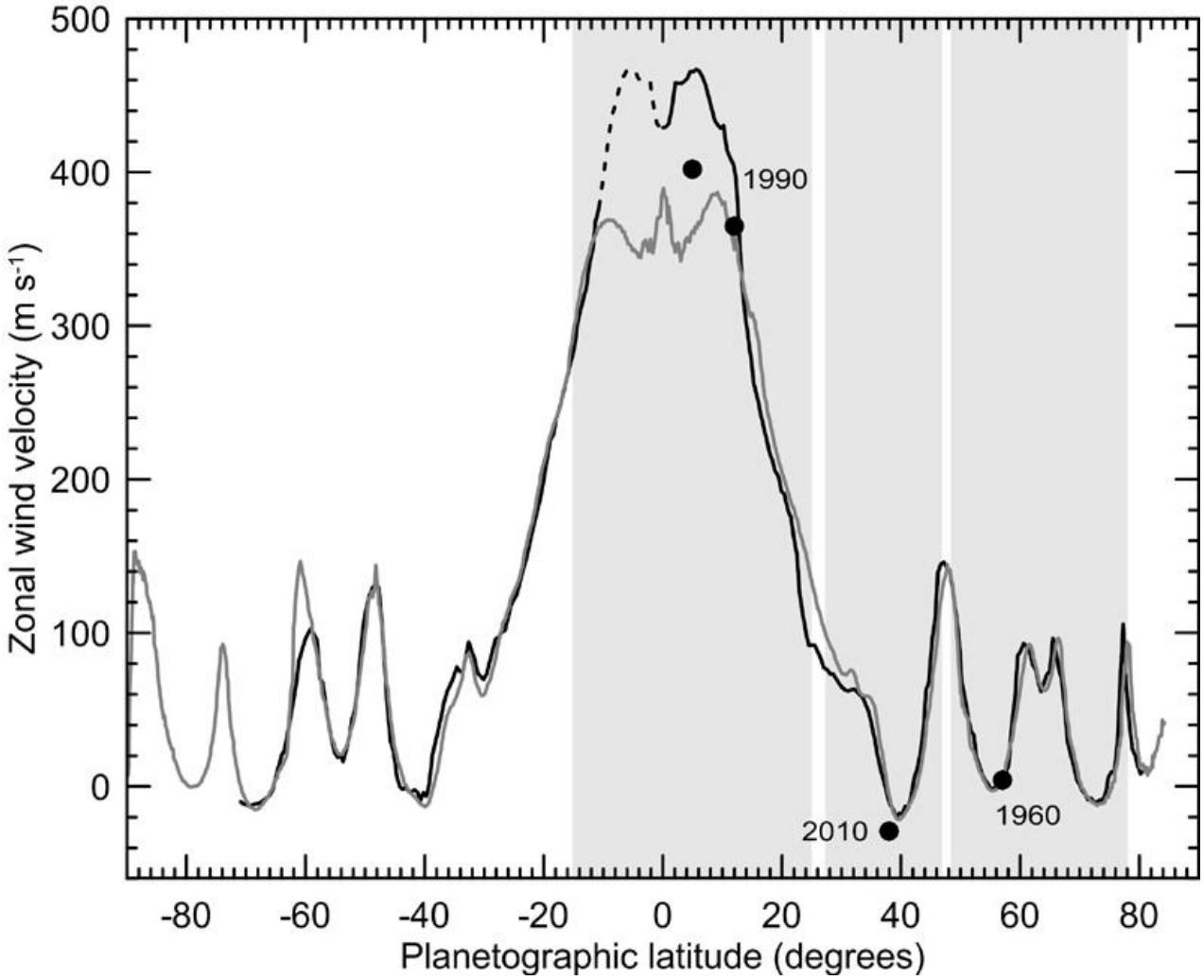

Figure 3 (electronic version)

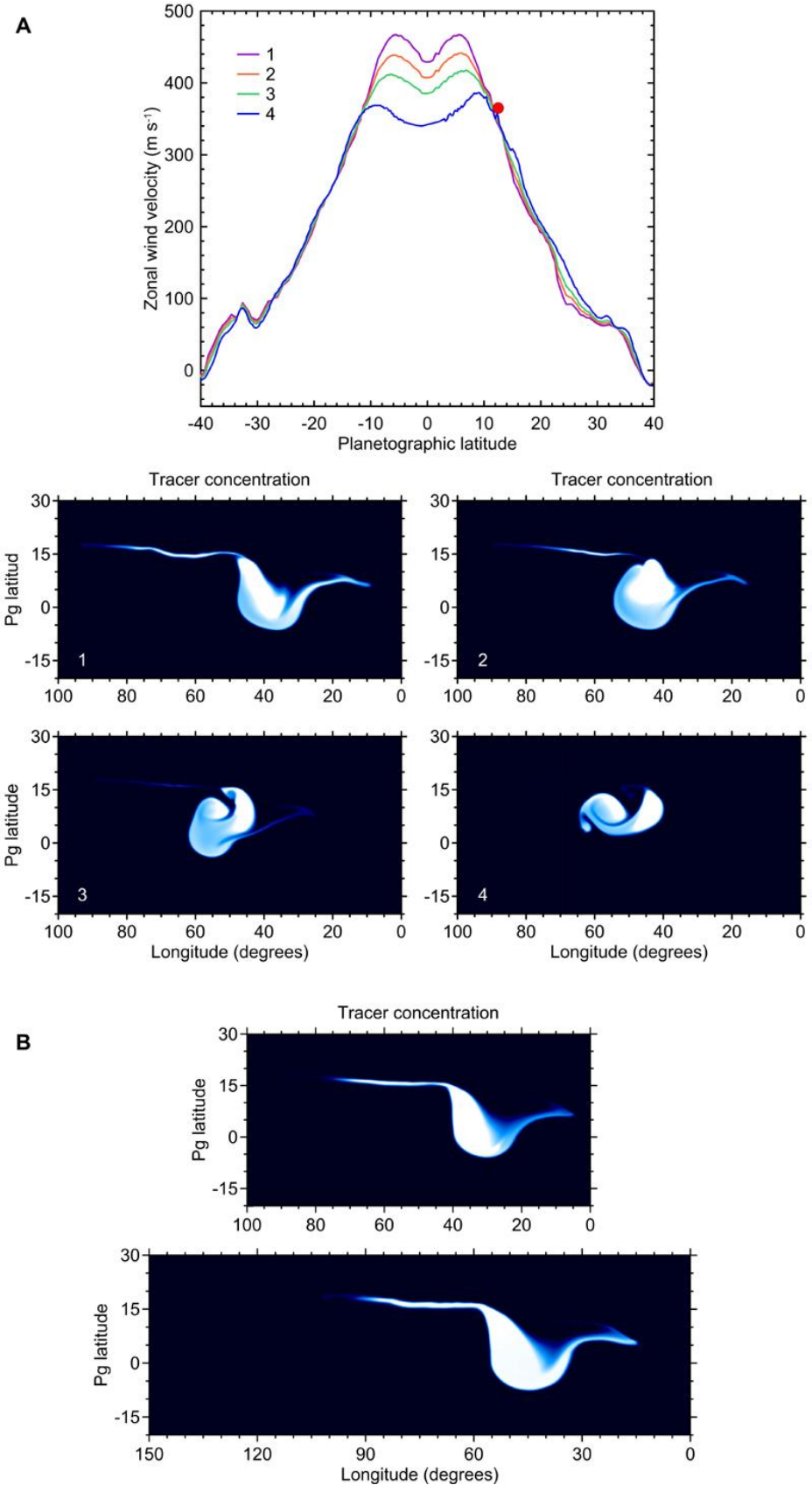

Figure 3 (printed version)

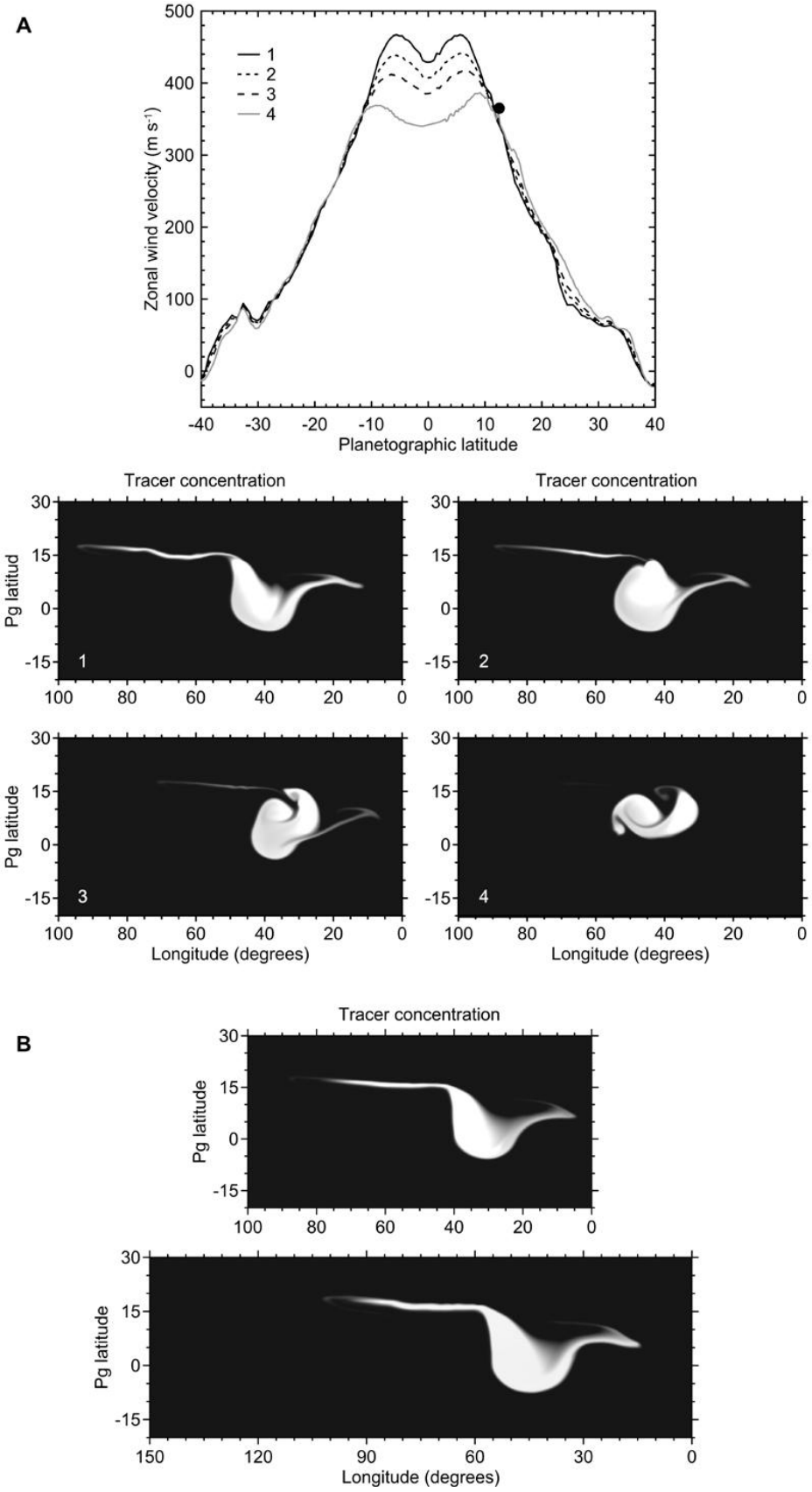

Figure 4 (electronic version)

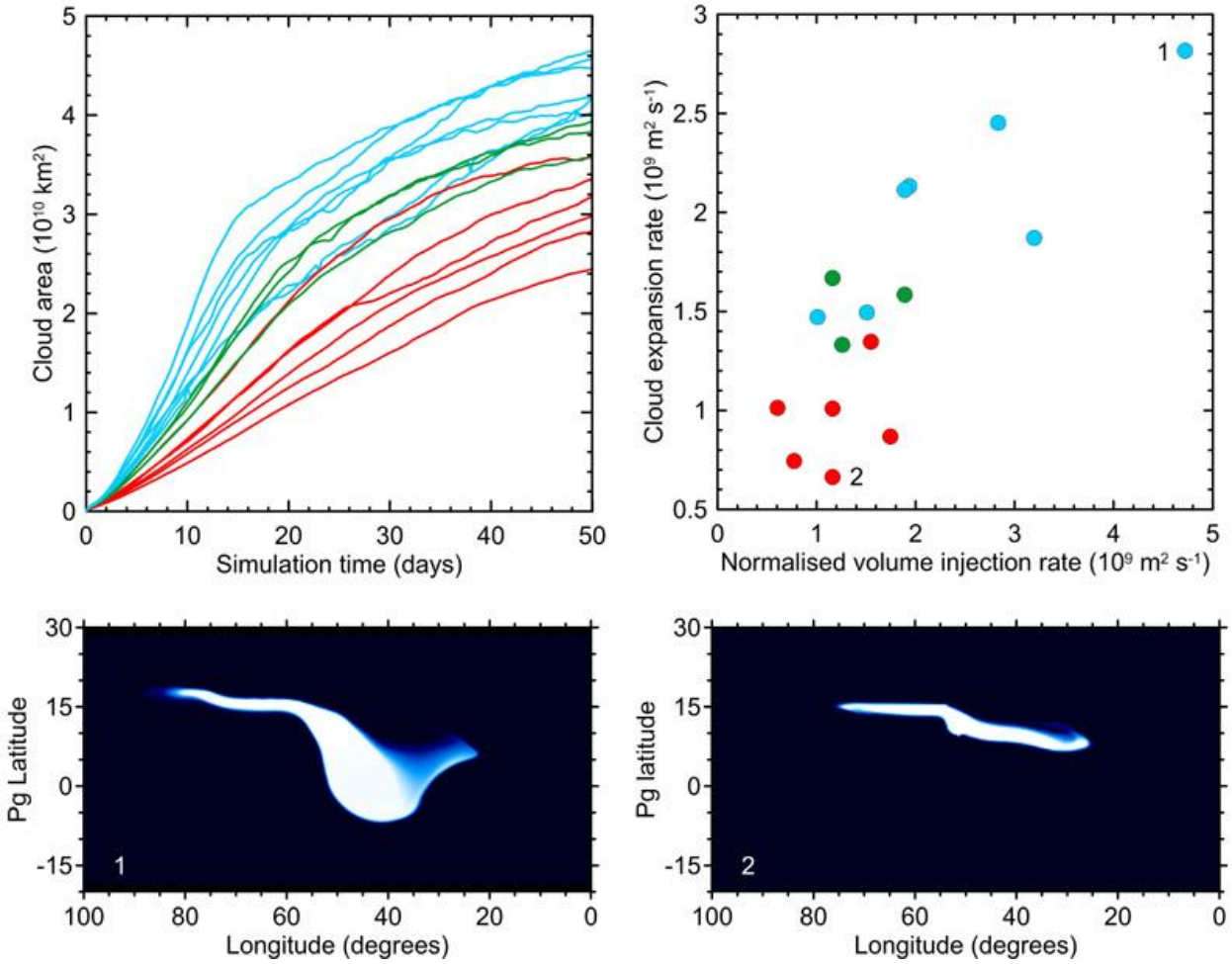

Figure 4 (printed version)

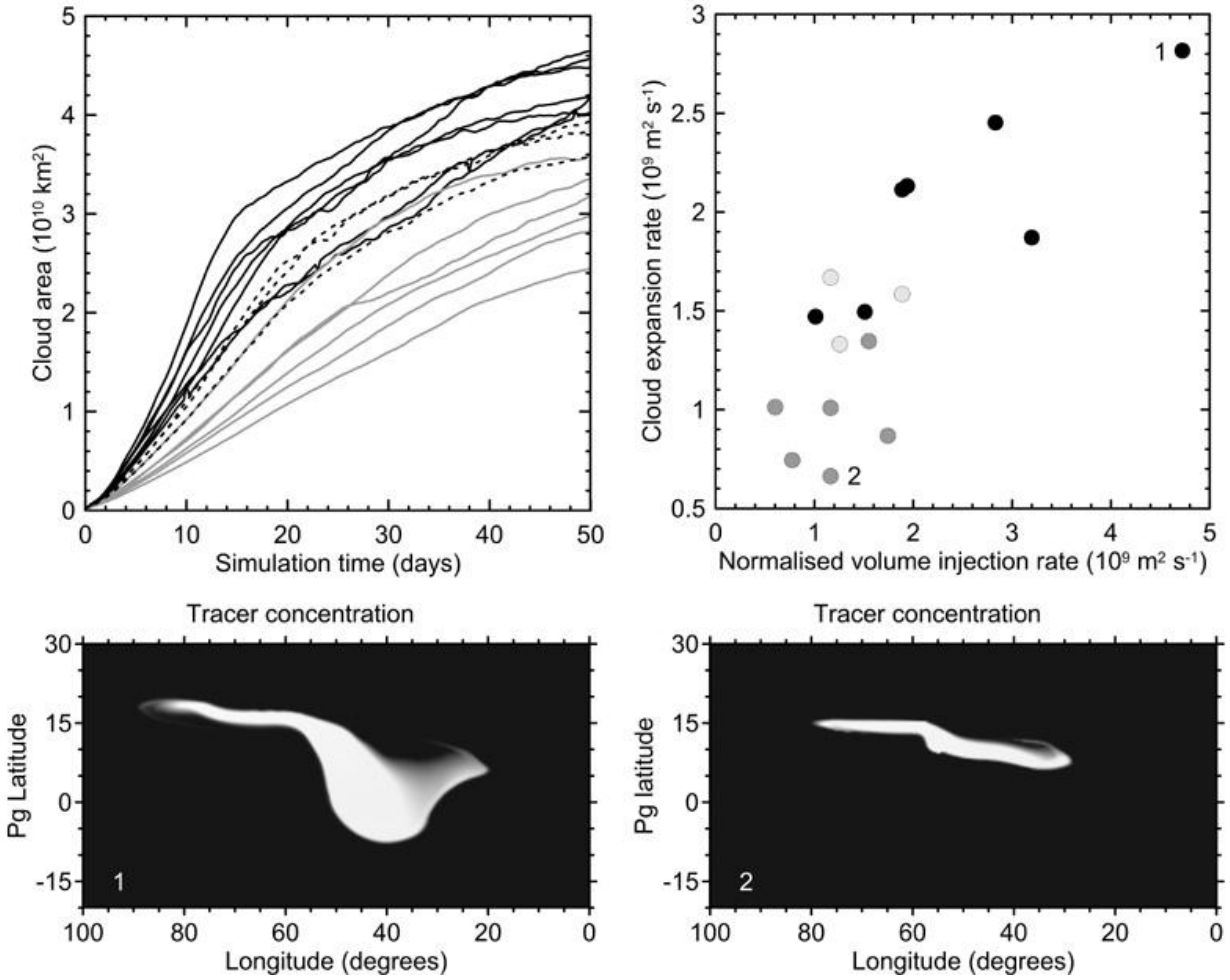

Figure 5 (electronic version)

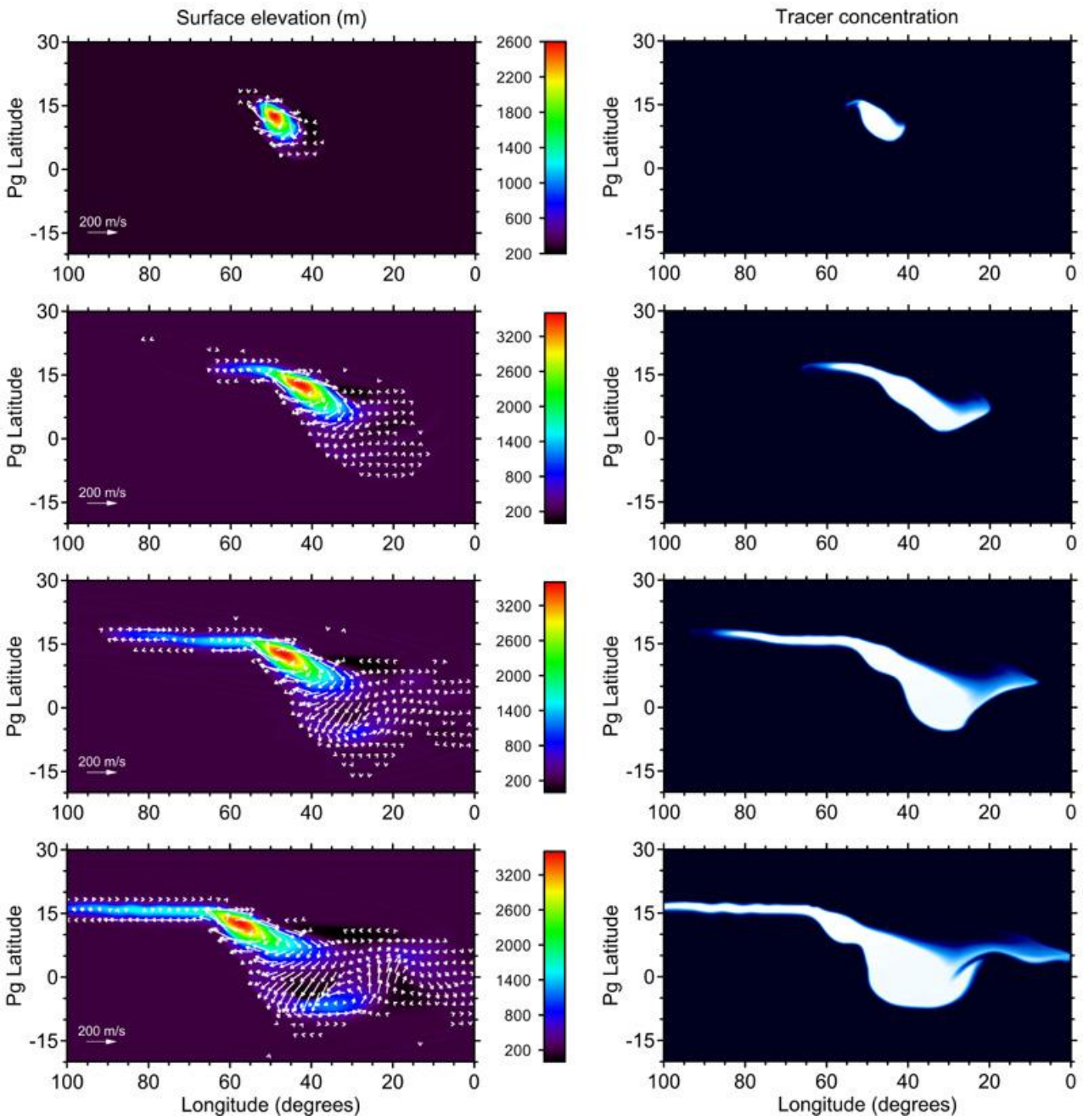

Figure 5 (printed version)

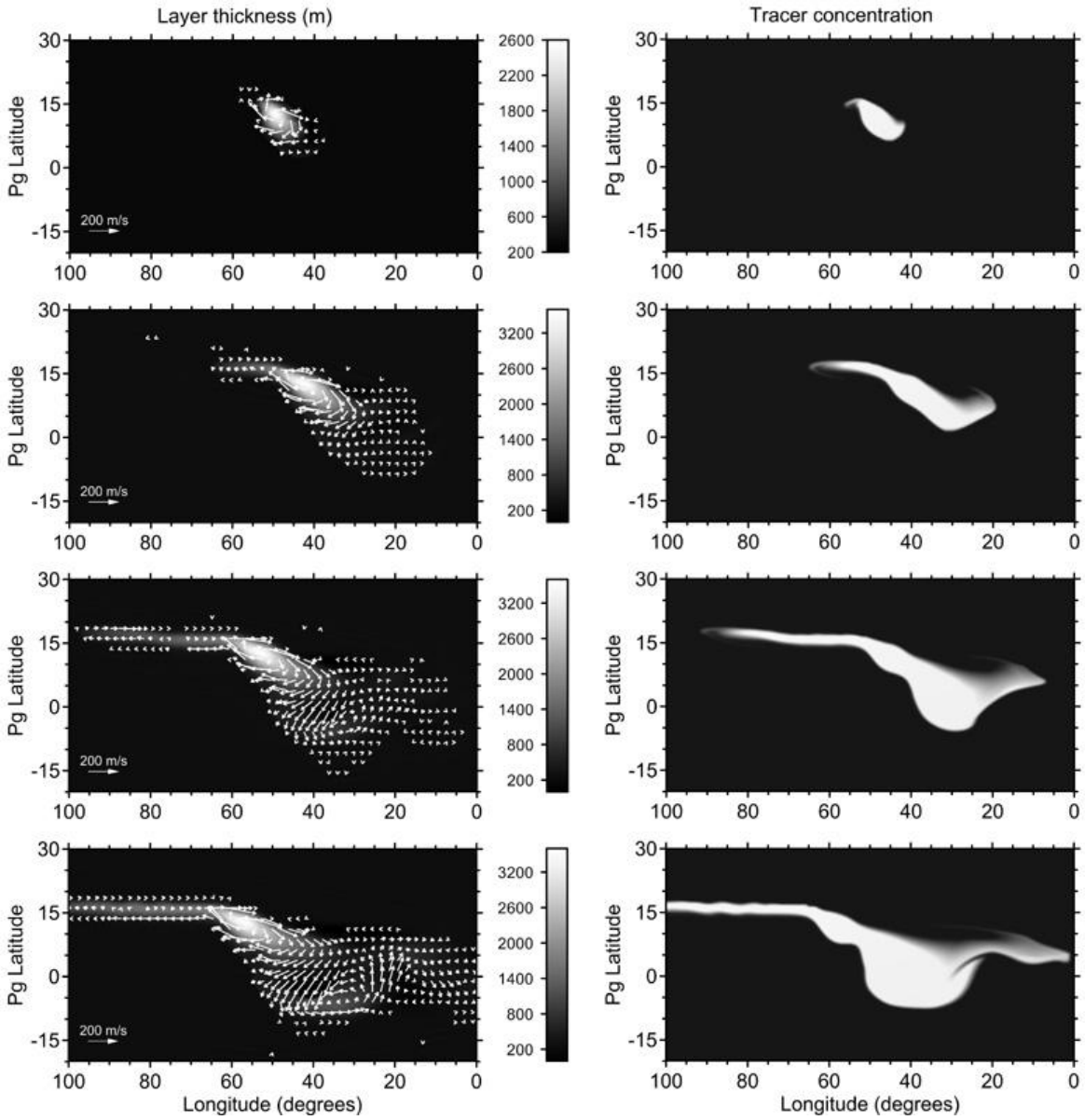

Figure 6 (electronic version)

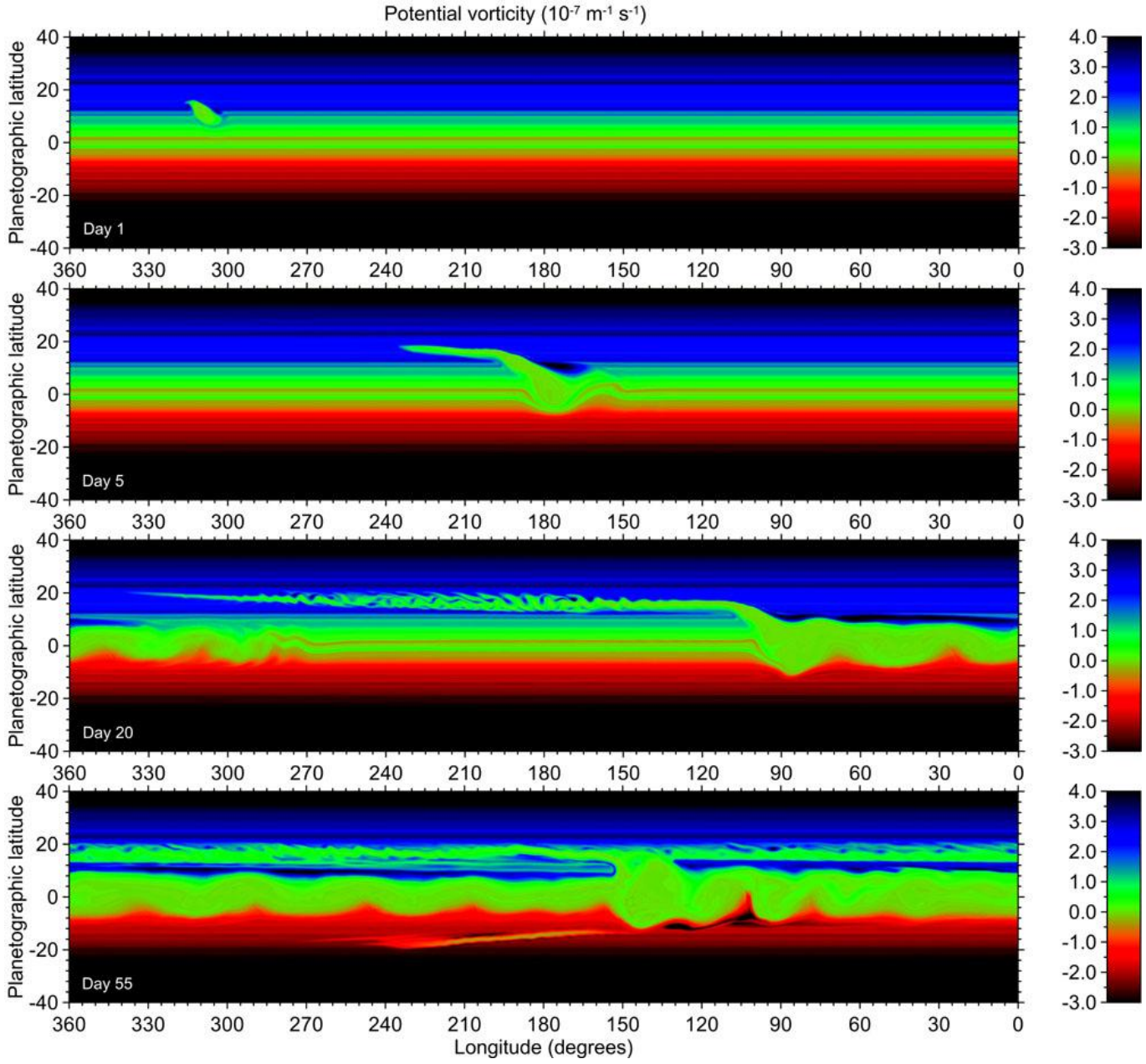

Figure 6 (printed version)

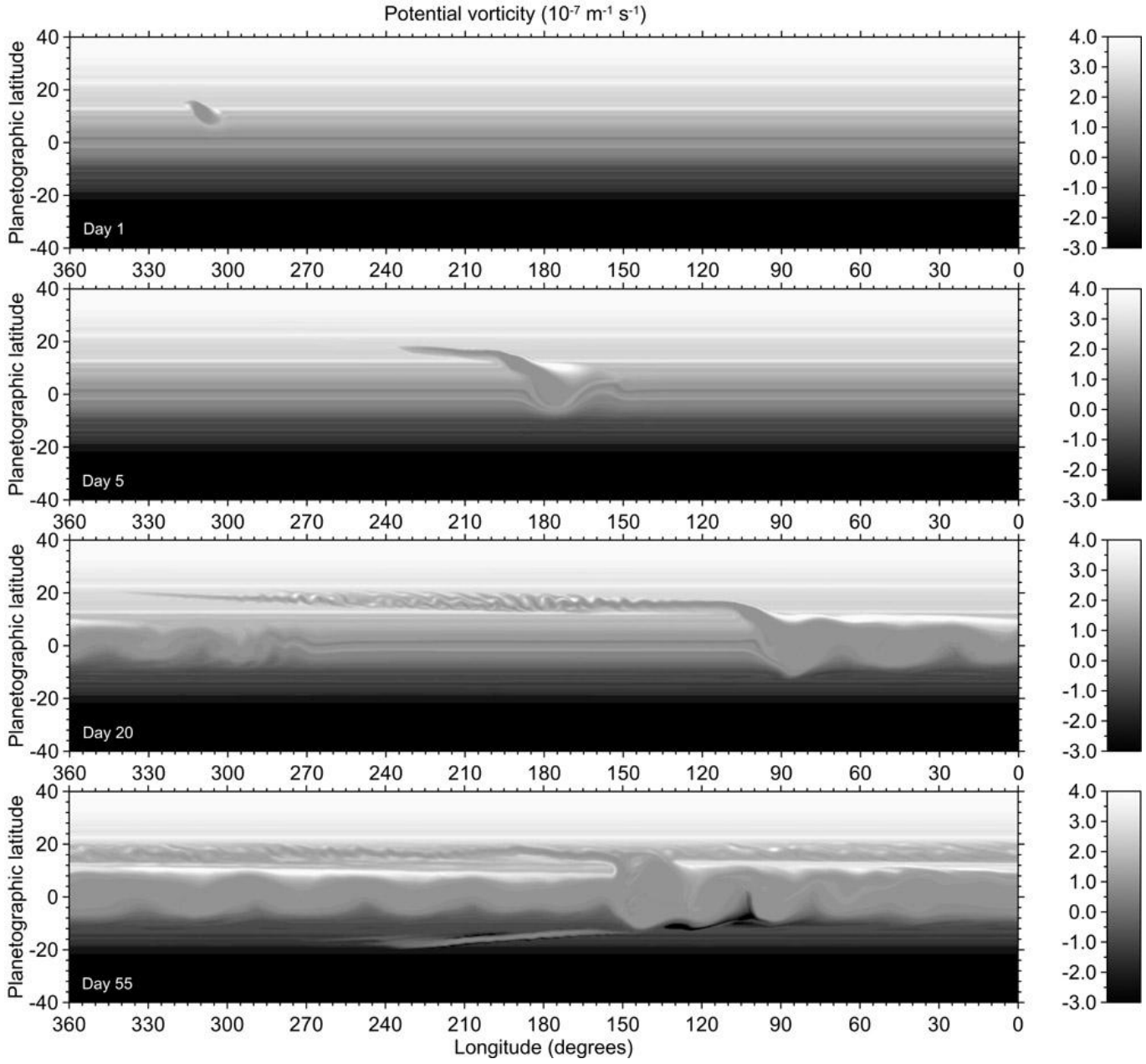

Figure 7 (electronic version)

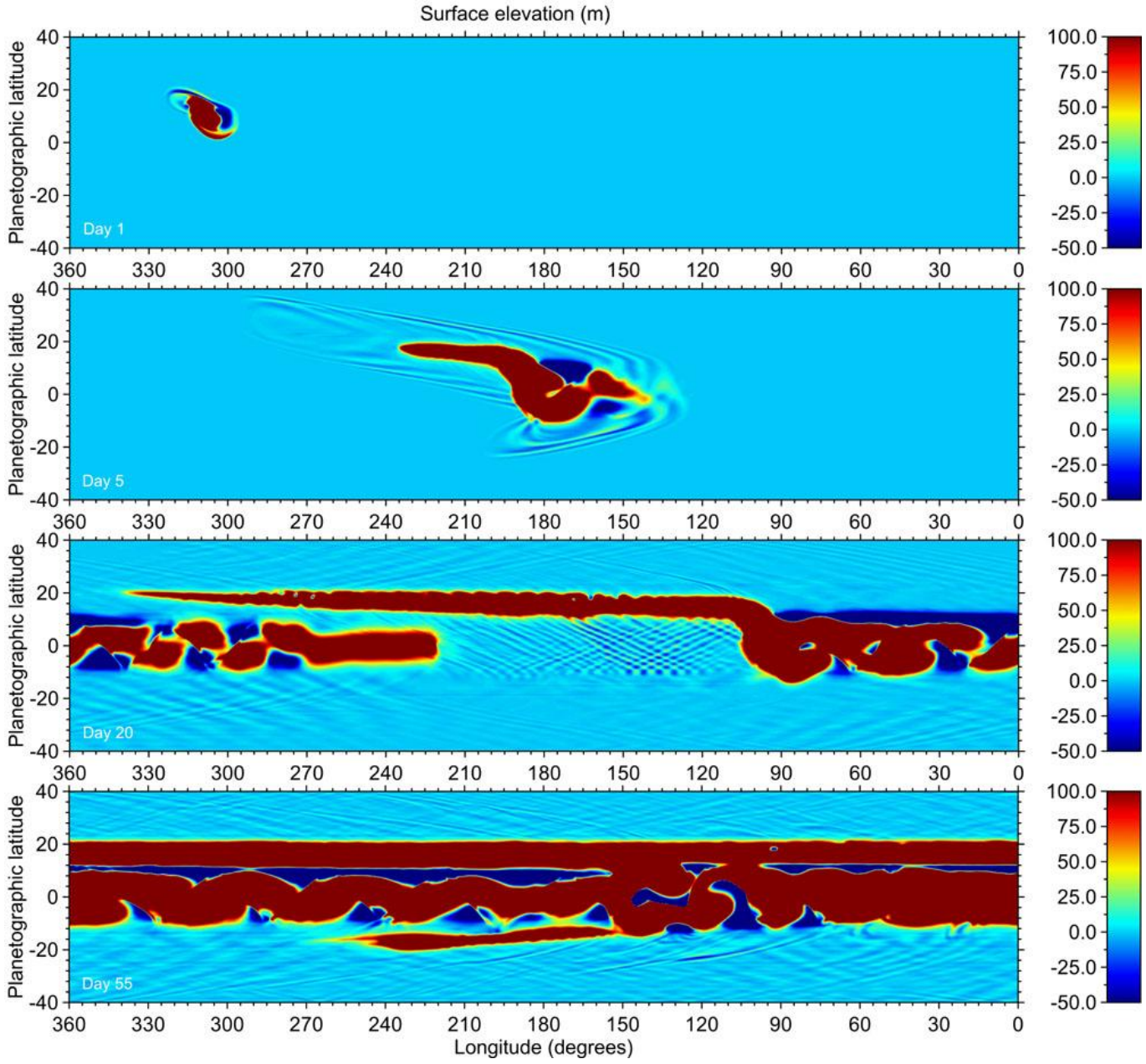

Figure 7 (printed version)

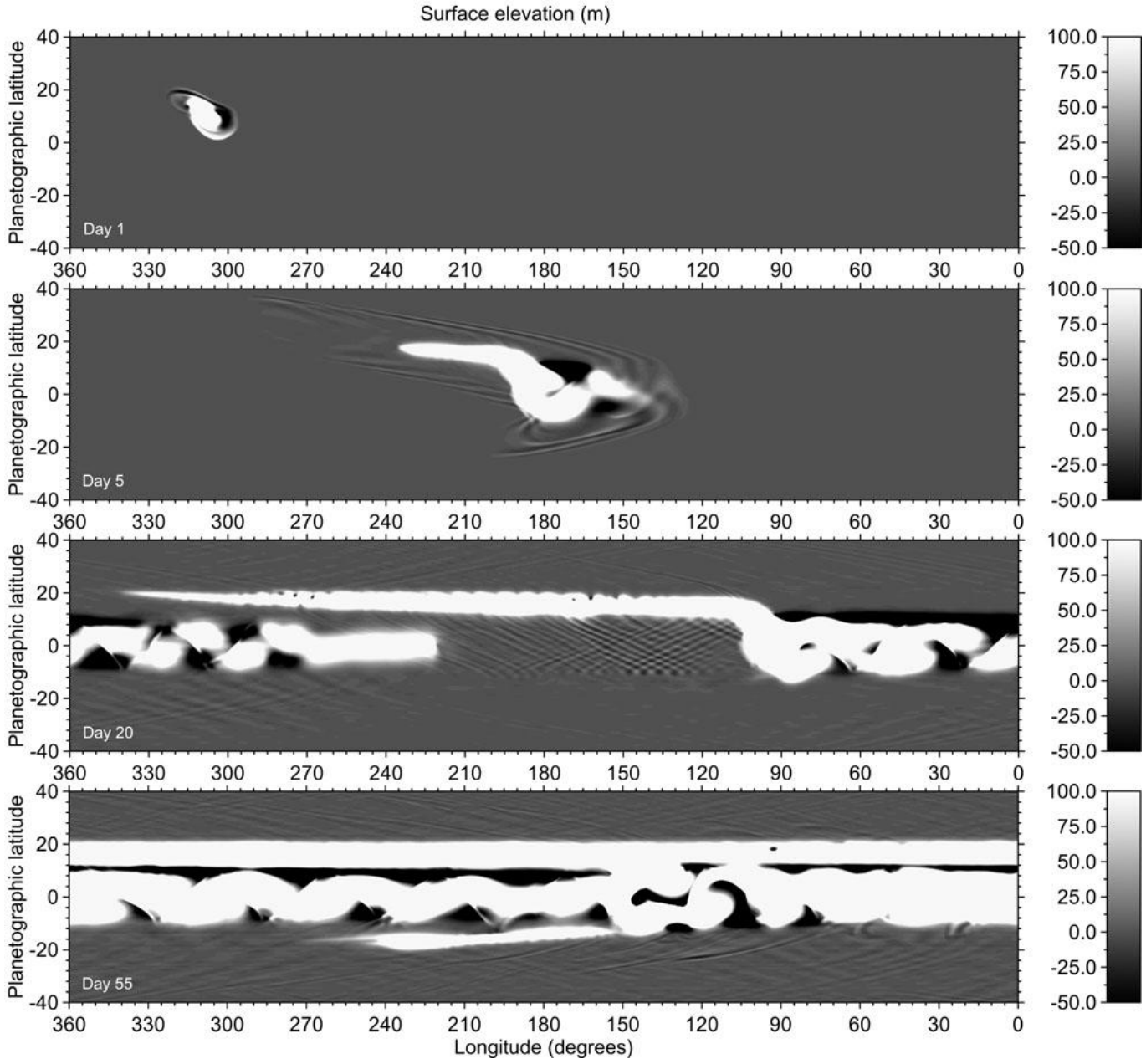

Figure 8 (electronic version)

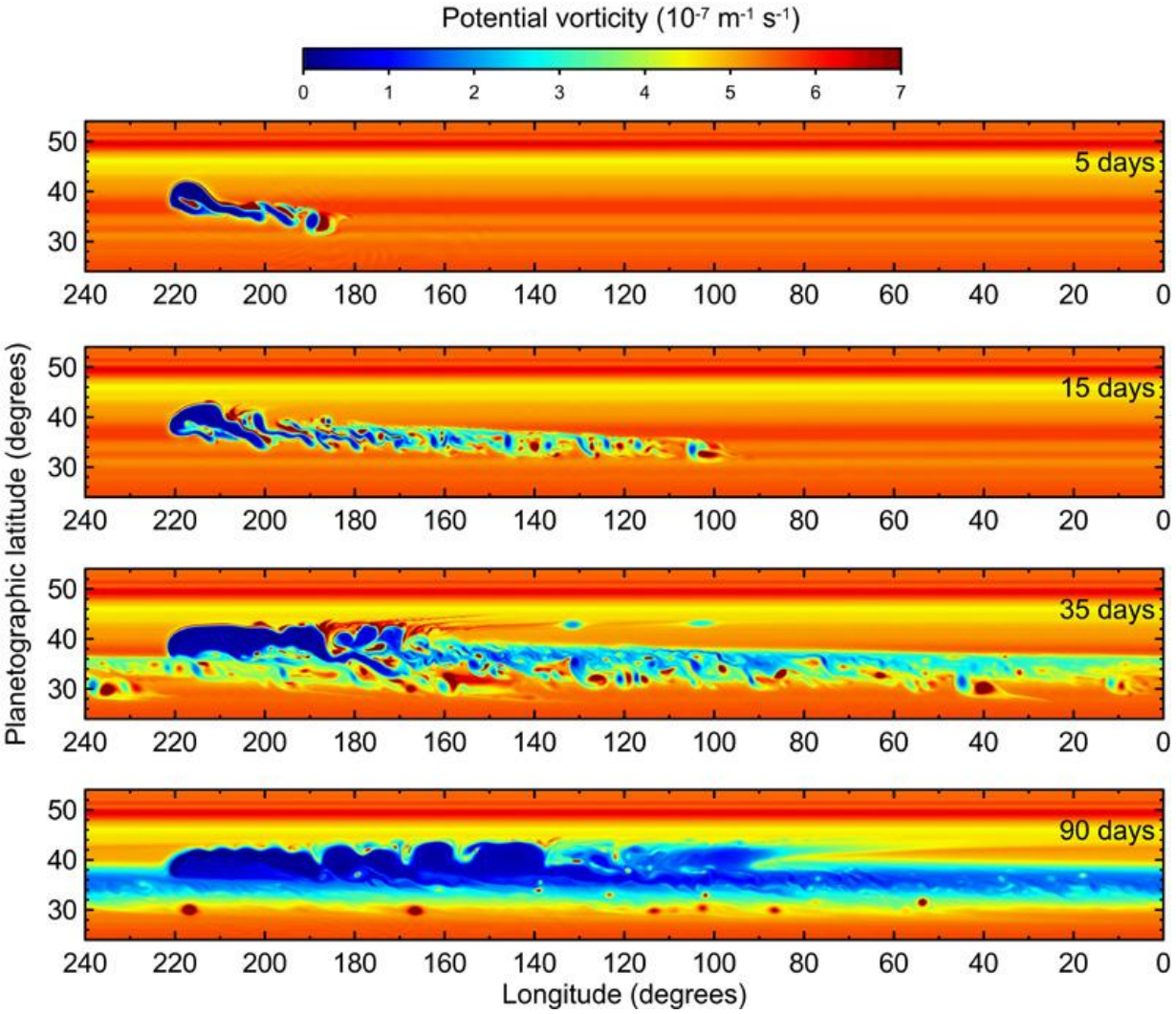

Figure 8 (printed version)

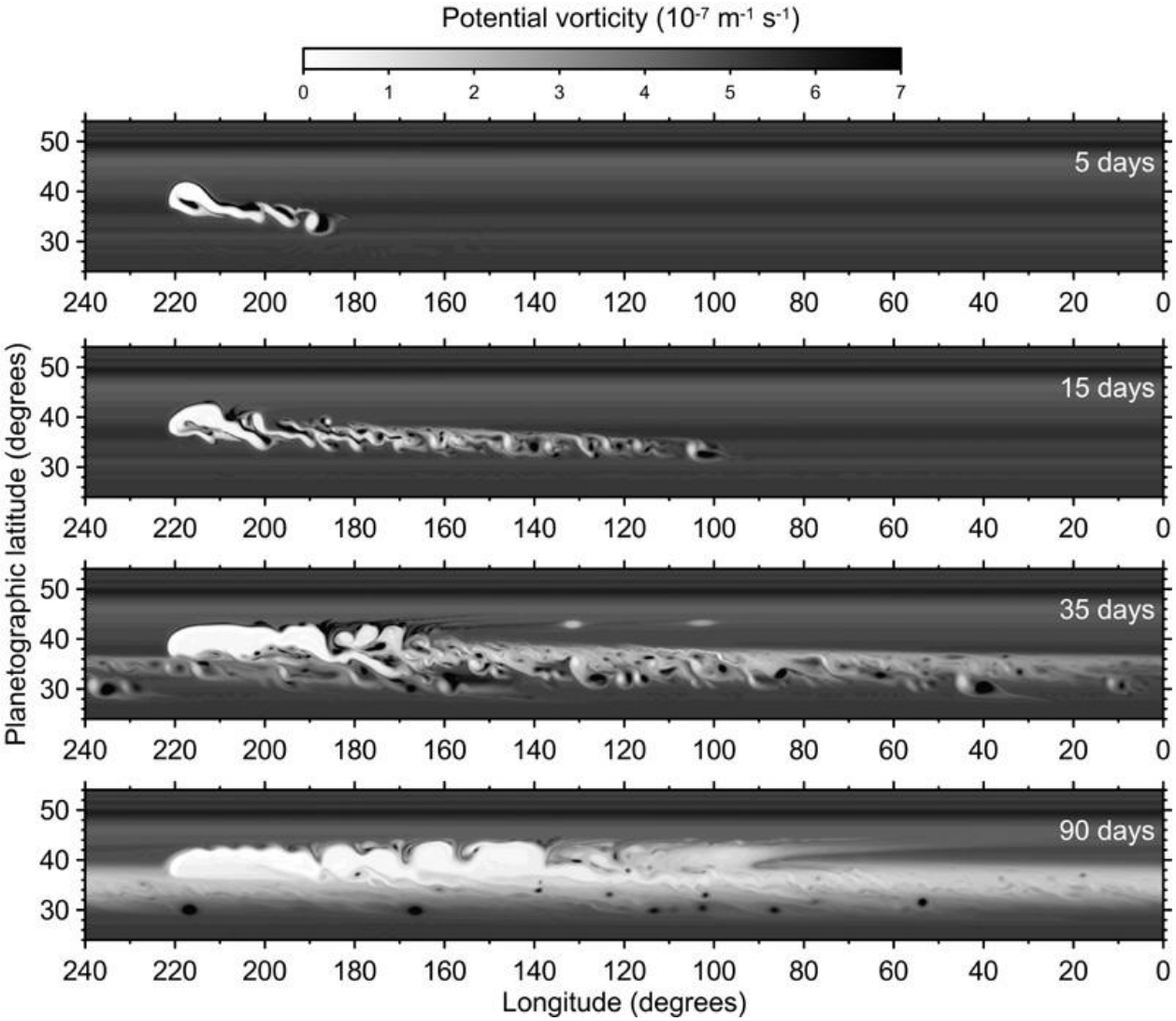

Figure 9 (electronic version)

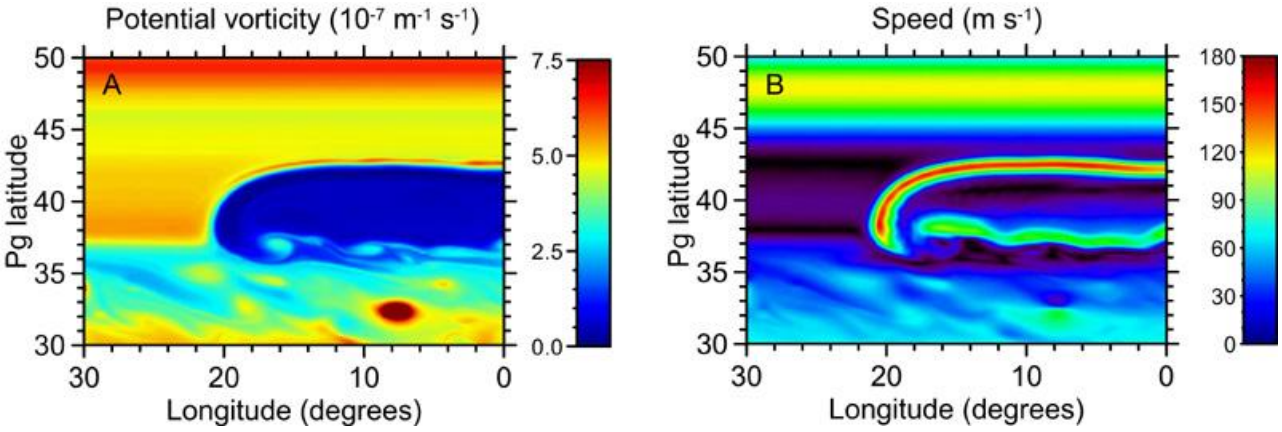

Figure 9 (printed version)

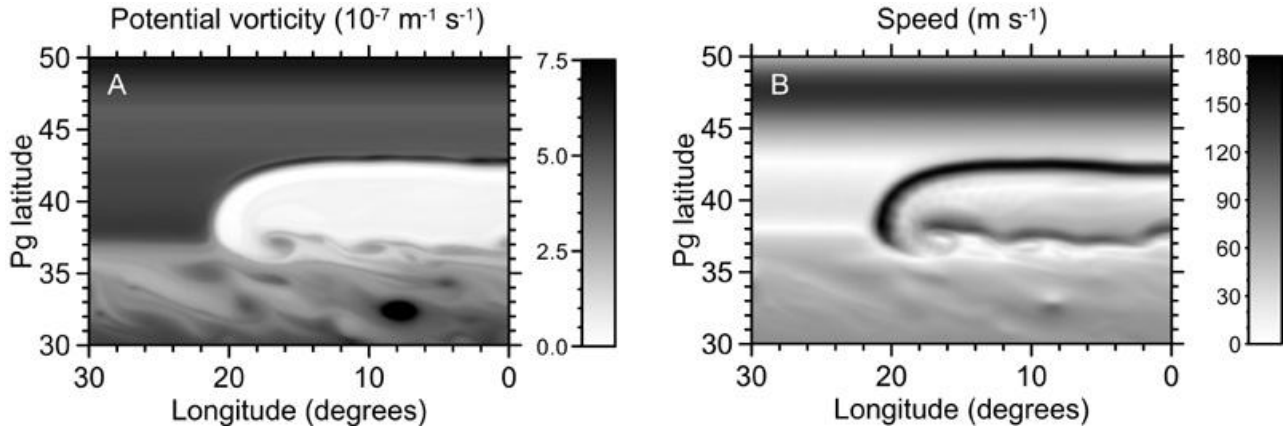

Figure 10 (electronic & printed versions)

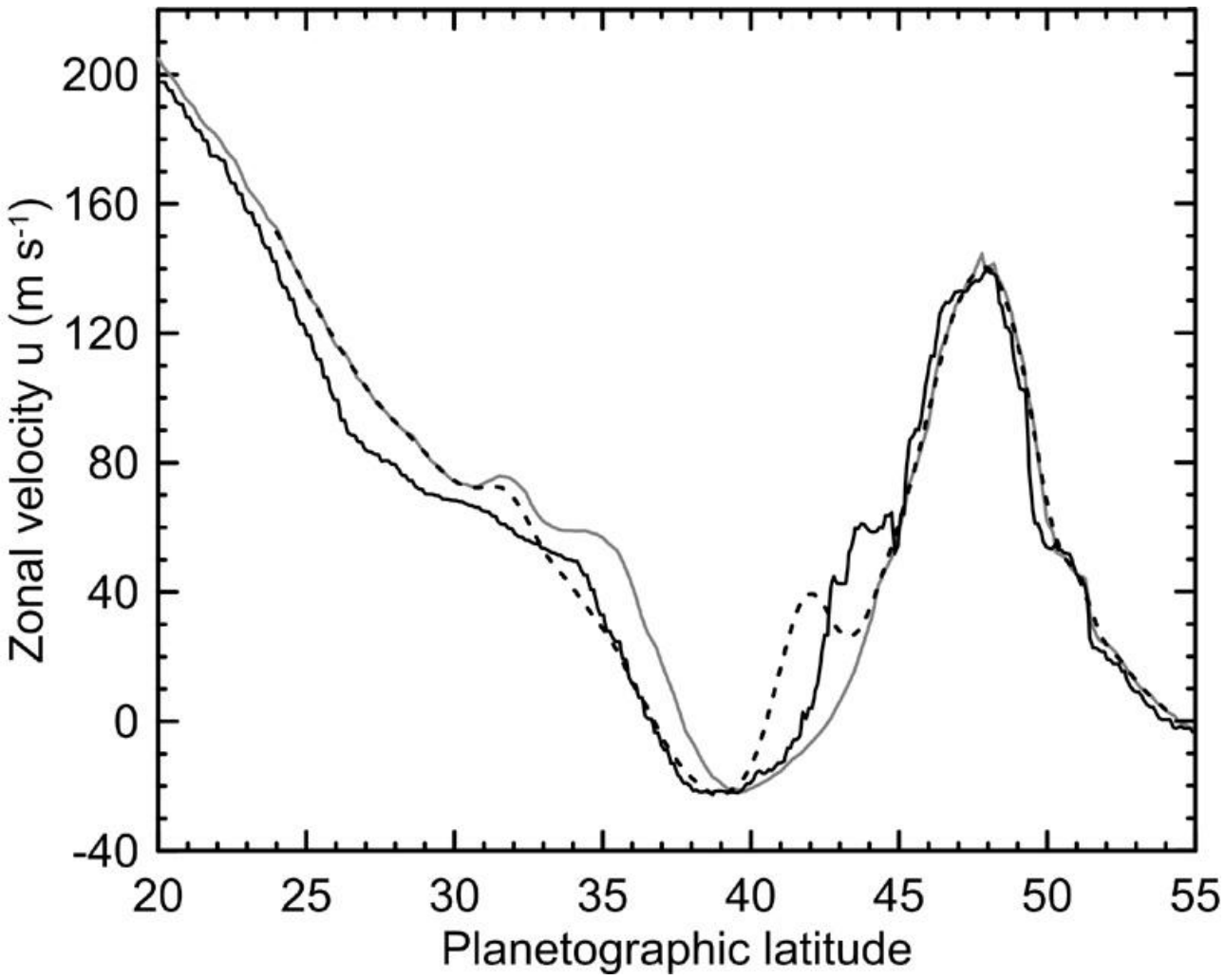

Figure 11 (electronic & printed versions)

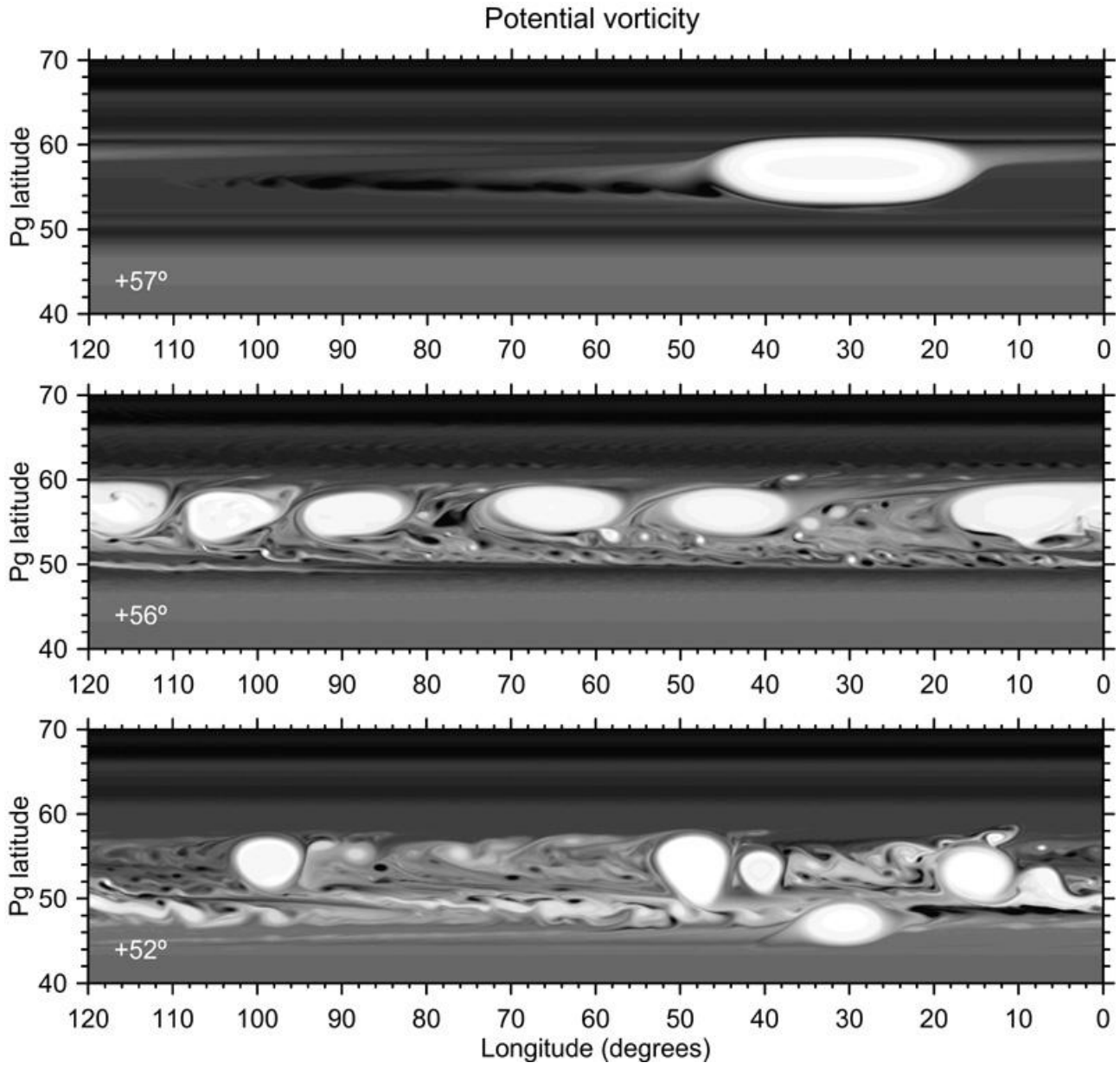

Figure A.1 (electronic version)

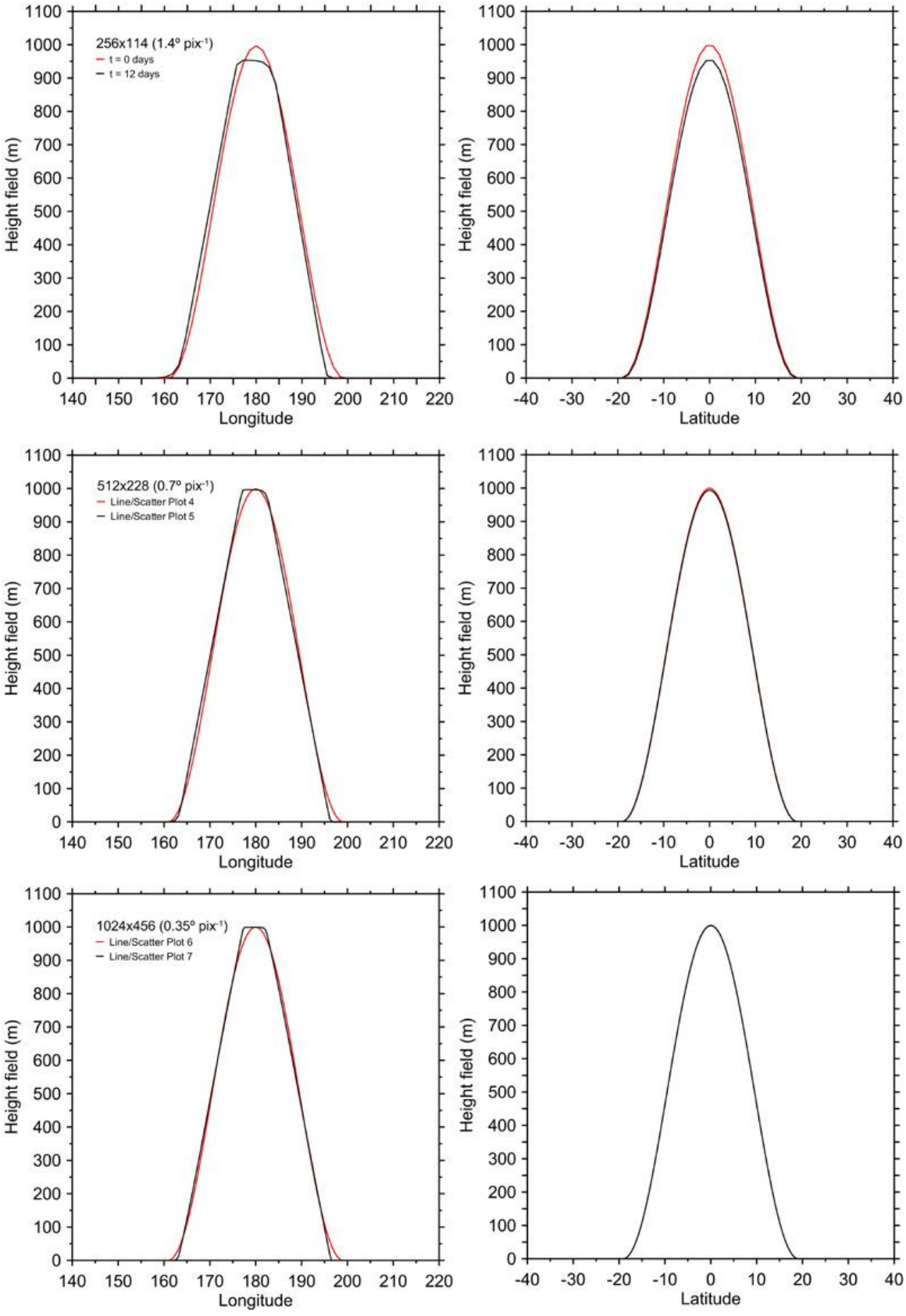

Figure A.1 (printed version)

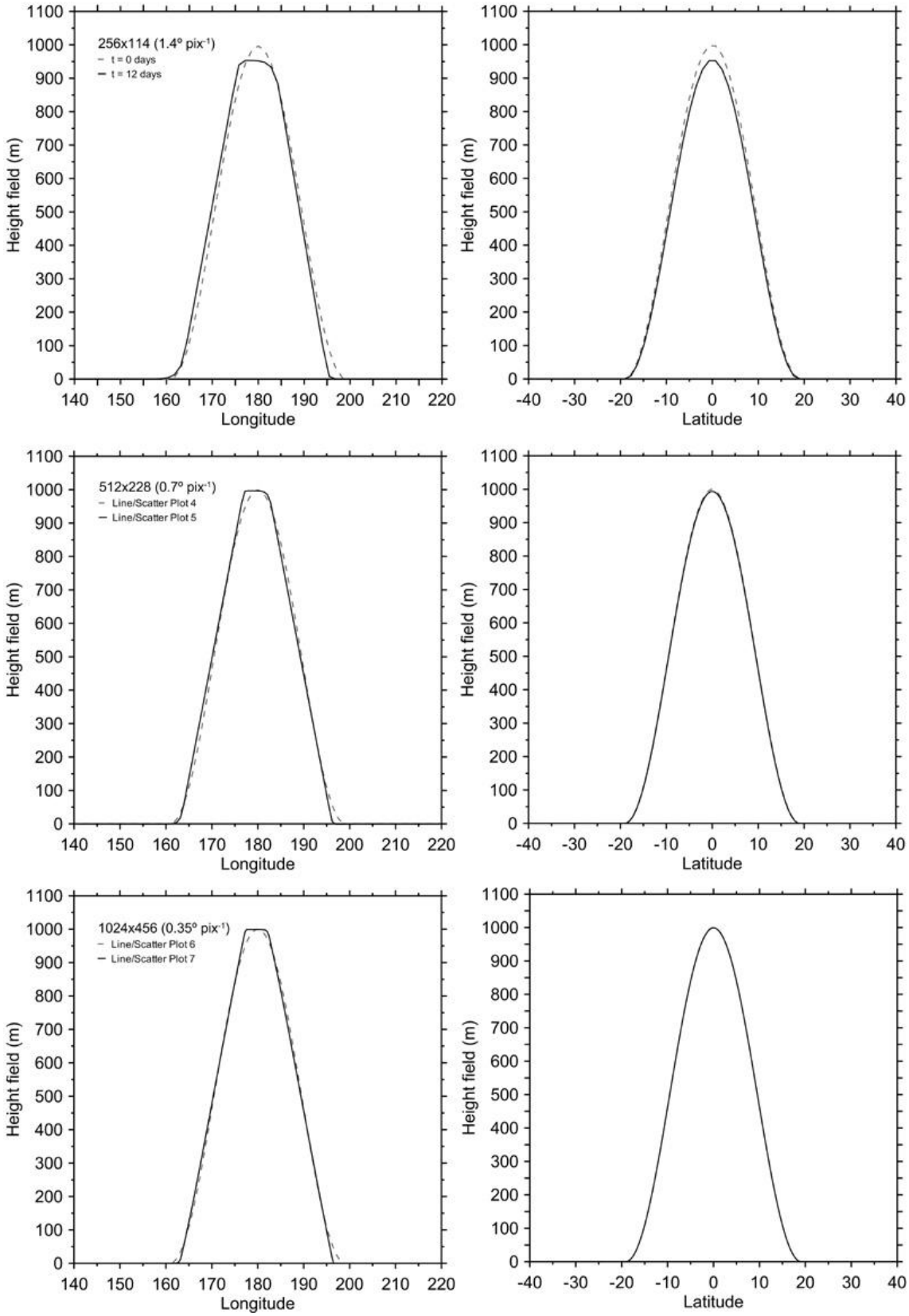

Figure A.2 (electronic & printed versions)

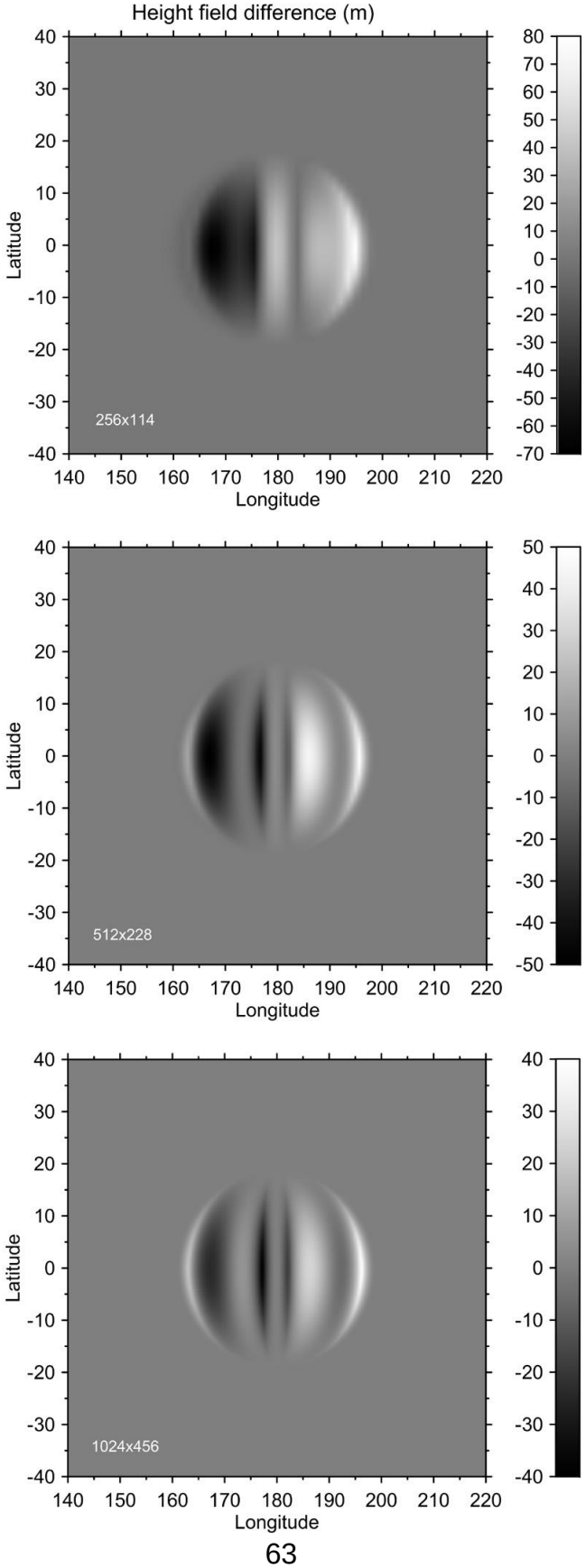

Figure A.3 (electronic version)

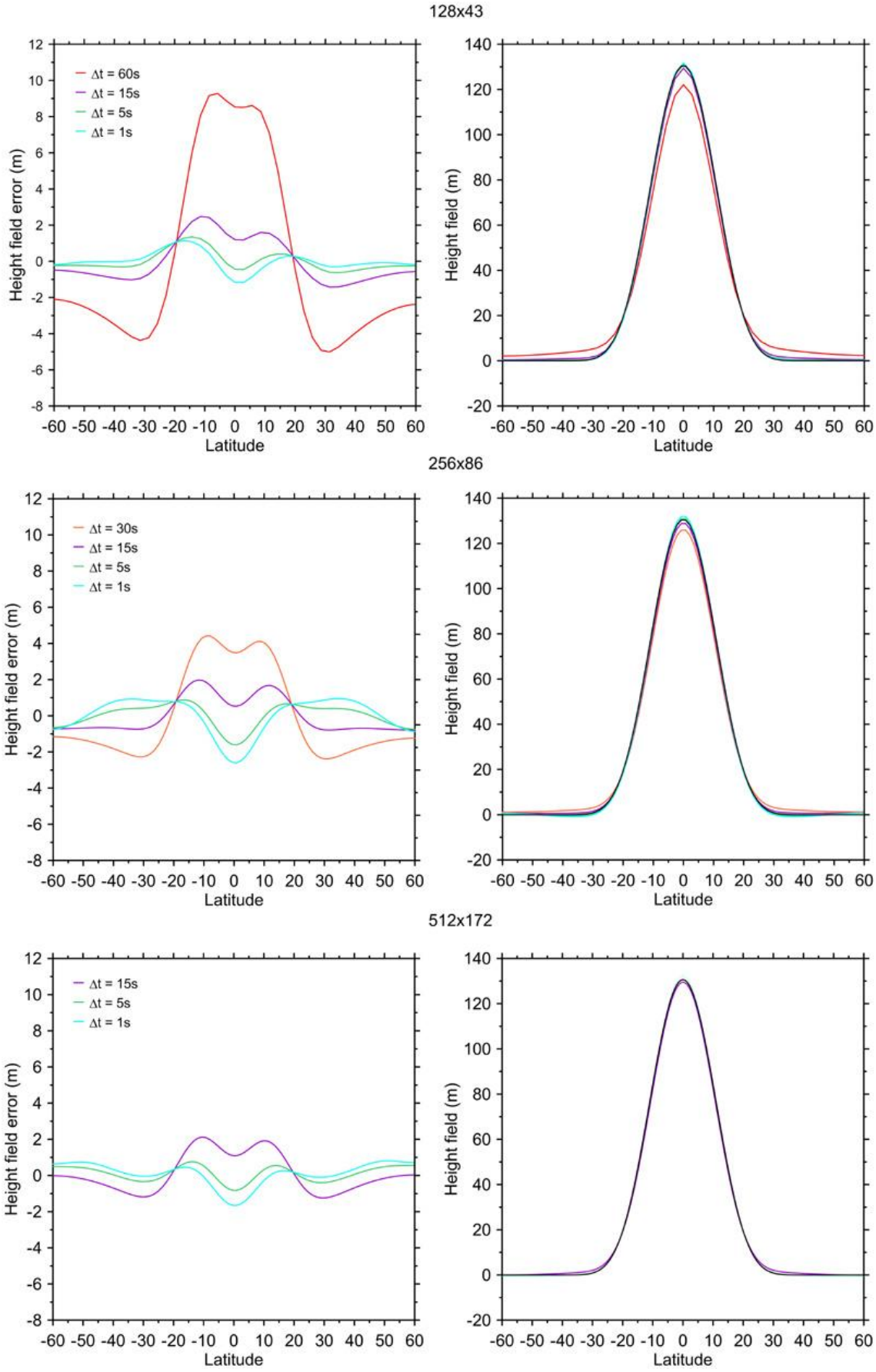

Figure A.3 (printed version)

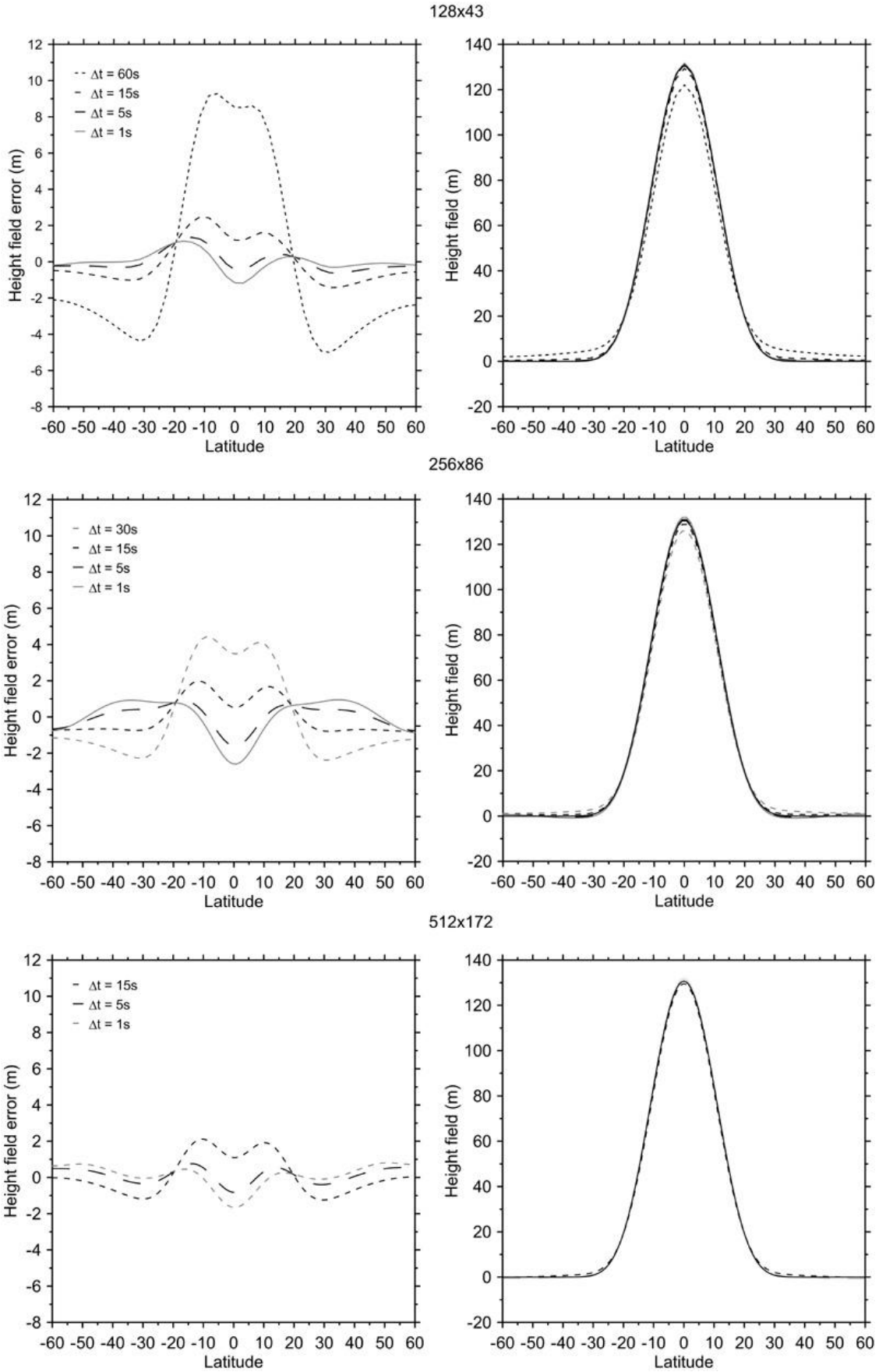

Figure A.4 (electronic version)

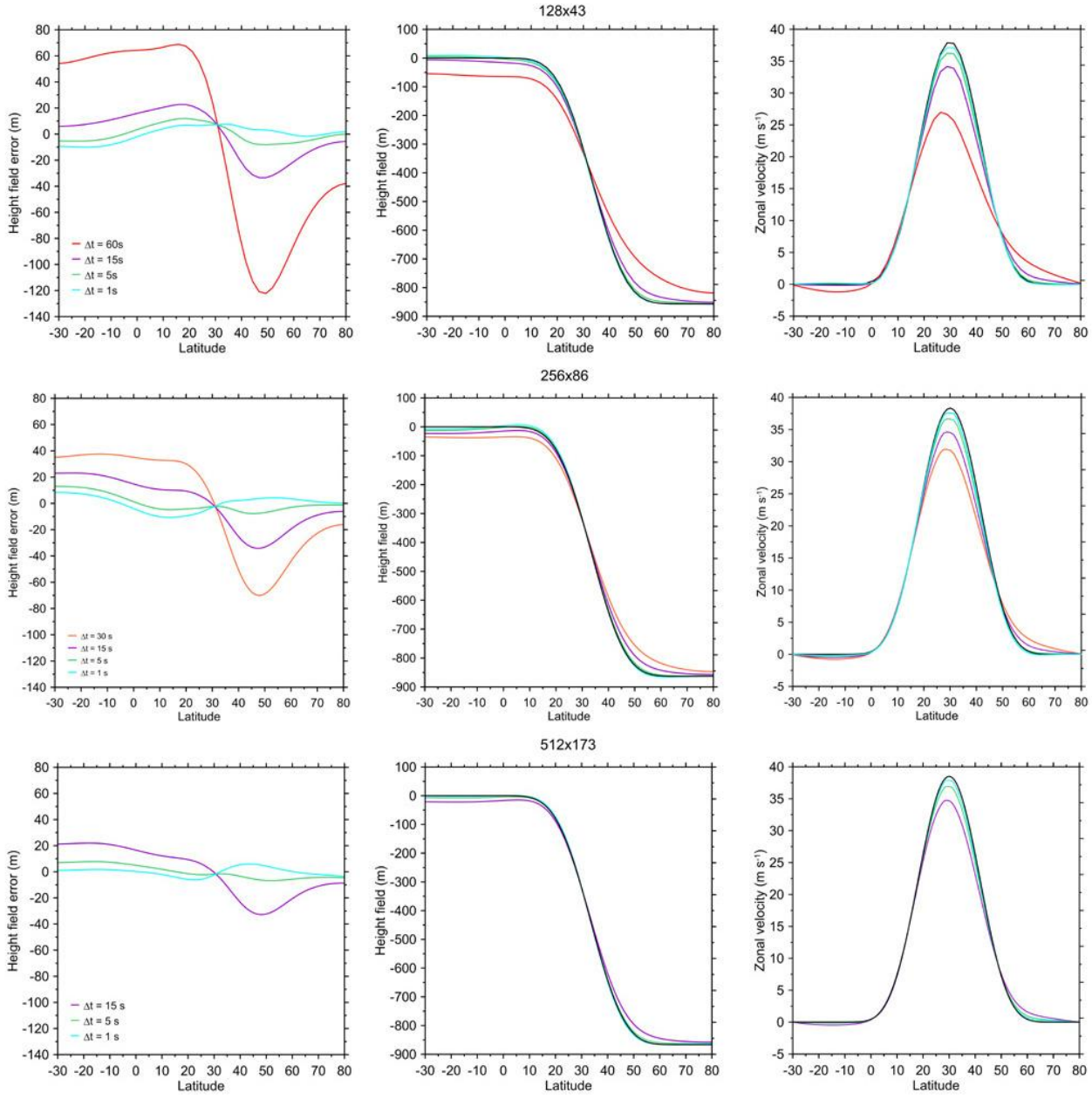

Figure A.4 (printed version)

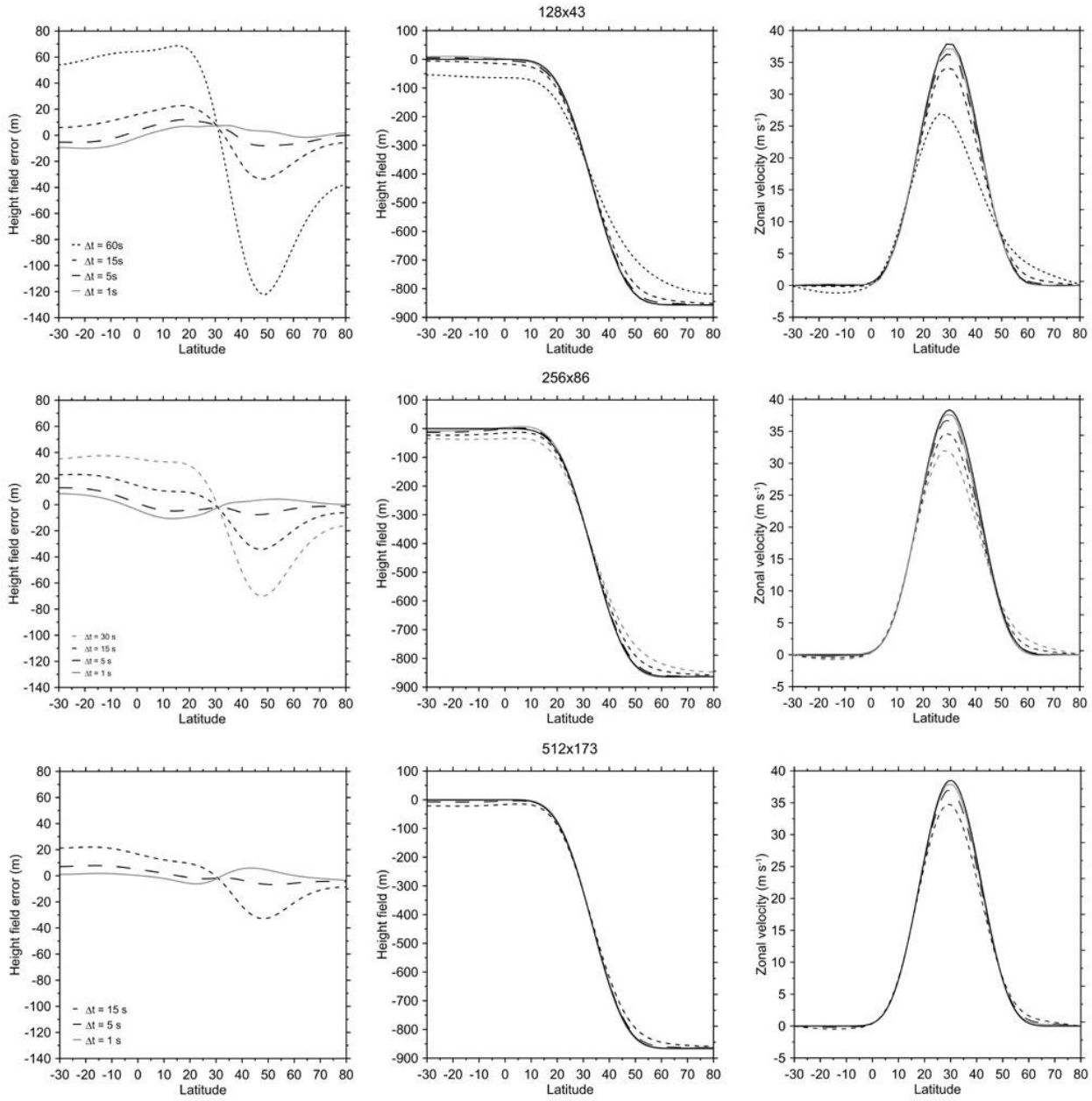

Figure A.5 (electronic and printed versions)